JEM Journal of Experimental Medicine

ARTICLE

Skin mesenchymal niches maintain and protect AML-initiating stem cells

Lakshmi Sandhow[1], Huan Cai[1]*, Elory Leonard[1]*, Pingnan Xiao[1], Luana Tomaipitinca[1], Alma Månsson[1], Makoto Kondo[1], Xiaoyan Sun[2], Anne-Sofie Johansson[1], Karl Tryggvason[3], Maria Kasper[2], Marcus Järås[4], and Hong Qian[1]

Leukemia cutis or leukemic cell infiltration in skin is one of the common extramedullary manifestations of acute myeloid leukemia (AML) and signifies a poorer prognosis. However, its pathogenesis and maintenance remain understudied. Here, we report massive AML cell infiltration in the skin in a transplantation-induced *MLL-AF9* AML mouse model. These AML cells could regenerate AML after transplantation. Prospective niche characterization revealed that skin harbored mesenchymal progenitor cells (MPCs) with a similar phenotype as BM mesenchymal stem cells. These skin MPCs protected AML-initiating stem cells (LSCs) from chemotherapy in vitro partially via mitochondrial transfer. Furthermore, *Lama4* deletion in skin MPCs promoted AML LSC proliferation and chemoresistance. Importantly, more chemoresistant AML LSCs appeared to be retained in *Lama4*$^{-/-}$ mouse skin after cytarabine treatment. Our study reveals the characteristics and previously unrecognized roles of skin mesenchymal niches in maintaining and protecting AML LSCs during chemotherapy, meriting future exploration of their impact on AML relapse.

Introduction

Leukemia cutis (leukemic cell infiltration in skin) is one of the commonly observed extramedullary manifestations in acute myeloid leukemia (AML; Bakst et al., 2011; Gouache et al., 2018) and associated with poor survival (Gouache et al., 2018; Krooks and Weatherall, 2018; Wang et al., 2019). However, our understanding of its pathogenesis is very limited. This has been mainly due to lack of knowledge about the extramedullary niches where AML cells infiltrate and are maintained.

For decades, great efforts have been put to elucidate the contribution of the hematopoietic niche in bone marrow (BM) to normal and malignant hematopoiesis. The BM niche consists of various types of cells including mesenchymal stem cells (MSCs), mesenchymal progenitor cells (MPCs), osteoblasts, and endothelial cells. Accumulating evidence has shown that BM MSCs and MPCs play important roles in maintaining normal hematopoiesis and in the development of myeloid malignancies, including AML (Hoggatt et al., 2016; Xiao et al., 2018b). Molecular alterations in these niches could lead to malignant transformation of hematopoietic cells (Dong et al., 2016; Raaijmakers et al., 2010; Xiao et al., 2018a). During leukemia development, the leukemic cells can alter the BM niche, which renders the niche to become favorable for leukemic cell growth but harmful for normal hematopoiesis (Hanoun et al., 2014; Jeong et al., 2018; Kim et al., 2015; Schepers et al., 2013; Xiao et al., 2018b). Using a *Cre-LoxP* mouse model allowing for selective deletion of the MSC population, we have shown that loss of MSCs accelerates AML progression (Hanoun et al., 2014; Xiao et al., 2018b). However, these markers are not unique for the mesenchymal cells in BM, thus it is not clear whether the mesenchymal cell niches in extramedullary organs like skin are also affected, thereby contributing to the AML progression.

Besides BM, extramedullary organs such as adipose tissue have been reported to accommodate hematopoietic stem and progenitor cells (HSPCs) in the stromal vascular fraction (Han et al., 2010). In blast crisis of chronic myeloid leukemia, the gonadal white adipose tissue is infiltrated by leukemic cells that adapt to the extramedullary niche and transform into resistant leukemia-initiating stem cells (LSCs) marked by CD36 expression (Ye et al., 2016). These findings indicate that extramedullary organs may serve as niches for HSPCs and LSCs.

[1]Department of Medicine Huddinge, Center for Hematology and Regenerative Medicine, Karolinska Institute, Karolinska University Hospital, Stockholm, Sweden; [2]Department of Cell and Molecular Biology, Karolinska Institute, Stockholm, Sweden; [3]Department of Medical Biochemistry and Biophysics, Karolinska Institute, Stockholm, Sweden; [4]Department of Clinical Genetics, Lund University, Lund, Sweden.

*H. Cai and E. Leonard contributed equally to this paper. Correspondence to Hong Qian: hong.qian@ki.se

M. Kondo's current affiliation is Department of Molecular Pharmaceutics, Health Sciences, Cell Sheet Tissue Engineering Center, University of Utah, Salt Lake City, UT, USA. P. Xiao's current affiliation is Bone Marrow Transplantation Center, the First Affiliated Hospital, Zhejiang University School of Medicine, Hangzhou, China.

Existing evidence suggests that skin might contain an MSC-like cell population (Kimlin and Virador, 2013; Toma et al., 2001; Vaculik et al., 2012; Viswanathan et al., 2019). However, their biological properties and contribution to hematopoiesis and leukemia remain unexplored. Knowledge of this would be essential for understanding the pathology of extramedullary leukemia in the skin and would thus provide new insights into identifying new potential therapeutic targets that may be translated into new treatment strategies for AML patients with leukemia cutis.

We, here in a transplantation-induced AML mouse model, detected massive infiltration of AML cells in the skin. Importantly, these skin AML cells at steady state or after chemotherapy could regenerate AML after secondary transplantation, even with a low dose of 10 cells/mouse. Characterization of the AML niche revealed the molecular features and developmental hierarchy of the skin MPCs. The MPCs expressing Early B cell Factor 2 (Ebf2) contribute to mesenchymal cell turnover in the skin and were reduced after AML onset. The skin MPCs could maintain and protect AML LSCs, and loss of *Lama4* in skin MPCs promoted AML cell proliferation and resistance to chemotherapy. Altogether, our study revealed the characteristics and a previously unrecognized role of skin MPCs in maintaining AML LSCs during AML development and chemotherapy.

Results

The AML cells infiltrated in skin can regenerate AML after transplantation

We have here studied extramedullary leukemia in skin by using an *MLL-AF9*$^+$ AML cell transplantation-induced AML mouse model (Fig. 1 A). After symptomatic AML onset (day 21–30 after transplantation), we detected the AML cell infiltration in the dorsal skin by fluorescence-activated cell sorting (FACS; Fig. 1, B–D) and hematoxylin and eosin staining (Fig. S1 A). The AML frequency was higher than that in the blood but lower than that in BM and spleen (Fig. 1, B and C). There was no clear correlation between the AML burden in skin and that in blood (Fig. S1 B, left). However, interestingly, the AML engraftment level in the skin correlated with a faster AML onset (Fig. 1 D) but not with the AML burden in blood (Fig. S1 B, right), pointing to a possible predicting value of AML cells in skin for AML progression. Confocal imaging showed that these AML cells mainly resided at perivascular sites in the skin (Fig. 1 E). The skin total cellularity was not affected (Fig. S1 C).

It is not known whether the AML cells infiltrated in skin contain LSCs capable of regenerating leukemia, particularly after chemotherapy. We, therefore, analyzed the AML cells in the skin 3 d after 5-d treatment with cytarabine (Ara-C)/normal saline (NS) or at the endpoint when the mice became moribund (Fig. 1 F). The AML engraftment in skin remained lower than that in BM and spleen after Ara-C treatment (Fig. 1 G and Fig. S1 D); however, there was no clear difference in the fraction of chemoresistant CD36$^+$ AML cells and colony-forming unit in culture (CFU-C) in the AML cells from different tissues (Fig. 1, H and I).

To functionally assess the frequency of the AML-initiating LSCs in the skin and BM, we sorted the AML cells from the primary recipient mice after Ara-C treatment (100 mg/Kg, daily) and performed secondary transplantation into non-irradiated mice in limiting dilution at doses of 10, 100, 1,000, and 5,000 cells per mouse (Fig. 1 F). The primary recipients treated with NS showed clear severe symptoms on days 22–33, resulting in ethical endpoint with an estimated median survival of 23.5 d. The median survival of the Ara-C–treated mice was 32 d (Fig. 1 J). The AML cells were sorted at 2–3 d after the last injection of Ara-C or NS. Notably, these AML cells in the skin could generate AML even at a low dose (10–100 cells/mouse; Fig. 1, J–O), as shown by the survival (Fig. 1 J), low-platelet counts (Fig. 1 K), splenomegaly (Fig. 1 L), and high AML engraftment in the BM at the endpoint (Fig. 1, M and N). Extreme limiting dilution analysis (Hu and Smyth, 2009) revealed that the frequency of residual AML-initiating LSCs in the skin (1/51) is similar to that in the BM (1/42) after Ara-C treatment but seemed to be somewhat higher than that (1/92) from the nontreated skin (Fig. 1 O). Given the higher AML cell frequency in the BM and spleen, the percentage of the AML-initiating LSCs and CFU-Cs in BM and spleen became higher than that in the skin (Fig. S1 E and Fig. 1 P). These data demonstrate the leukemia-initiating capacity of the AML cells in the skin tissue under steady state and after chemotherapy, indicating their potential impact on AML relapse.

Skin harbors Ebf2$^+$ and Ebf2$^-$ MPC subsets with similar immunophenotype to BM MSCs

To understand how the leukemic cells were maintained in the skin tissue, we explored the role of the extramedullary microenvironment in the skin using a similar approach as was used for characterizing the BM niche. BM MSCs have been shown to be involved in AML progression in mice (Xiao et al., 2018b). They are defined by a phenotype of lacking expression of CD44, hematopoietic (CD45/TER119), and endothelial (CD31) cell markers, but positive for PDGFRa/CD140a, SCA1, and CD51 (Morikawa et al., 2009; Pinho et al., 2013; Schepers et al., 2013; Xiao et al., 2018a; Xiao et al., 2018b). The primitive MSCs in mouse BM can be identified by Ebf2 expression (Qian et al., 2013) and can generate MSCs that lack Ebf2 (Xiao et al., 2018b). However, the phenotype of native skin MSCs remains unknown. The question is whether the cells with similar features exist in skin and play a role in AML cell maintenance under steady state and following chemotherapy. To answer this, we first characterized mesenchymal stem and progenitors in the skin by using the *Ebf2-Egfp* reporter mice. Similar to BM, a fraction of CD45$^-$TER119$^-$CD31$^-$ skin stromal cells expressed Ebf2 (Fig. 2 A). The Ebf2$^+$ cells accounted for about 2 and 5% of total live cells and CD45$^-$TER119$^-$CD31$^-$ stromal cells, respectively (Fig. 2, B and C). Phenotypically, skin Ebf2$^+$ cells highly expressed PDGFRa/CD140a and SCA1 (PαS) whereas about 41% of the Ebf2$^-$ cells were PαS cells (Fig. 2 D).

Functionally, both the Ebf2$^+$ and Ebf2$^-$ cells contained CFU in fibroblast (CFU-Fs), a colony-forming unit characteristic for MSCs (Fig. 2 E and Fig. S2 A). The CFU-Fs in the Ebf2$^+$ cells were generated exclusively by the SCA1$^+$ population (Fig. 2 F). Both Ebf2$^+$ and Ebf2$^-$PαS cell populations showed similar proliferation kinetics after passages 5–6 (Fig. S2 B) and were able to differentiate toward osteogenic and adipogenic lineages in vitro albeit to a different degree (Fig. S2, C and D). However, they

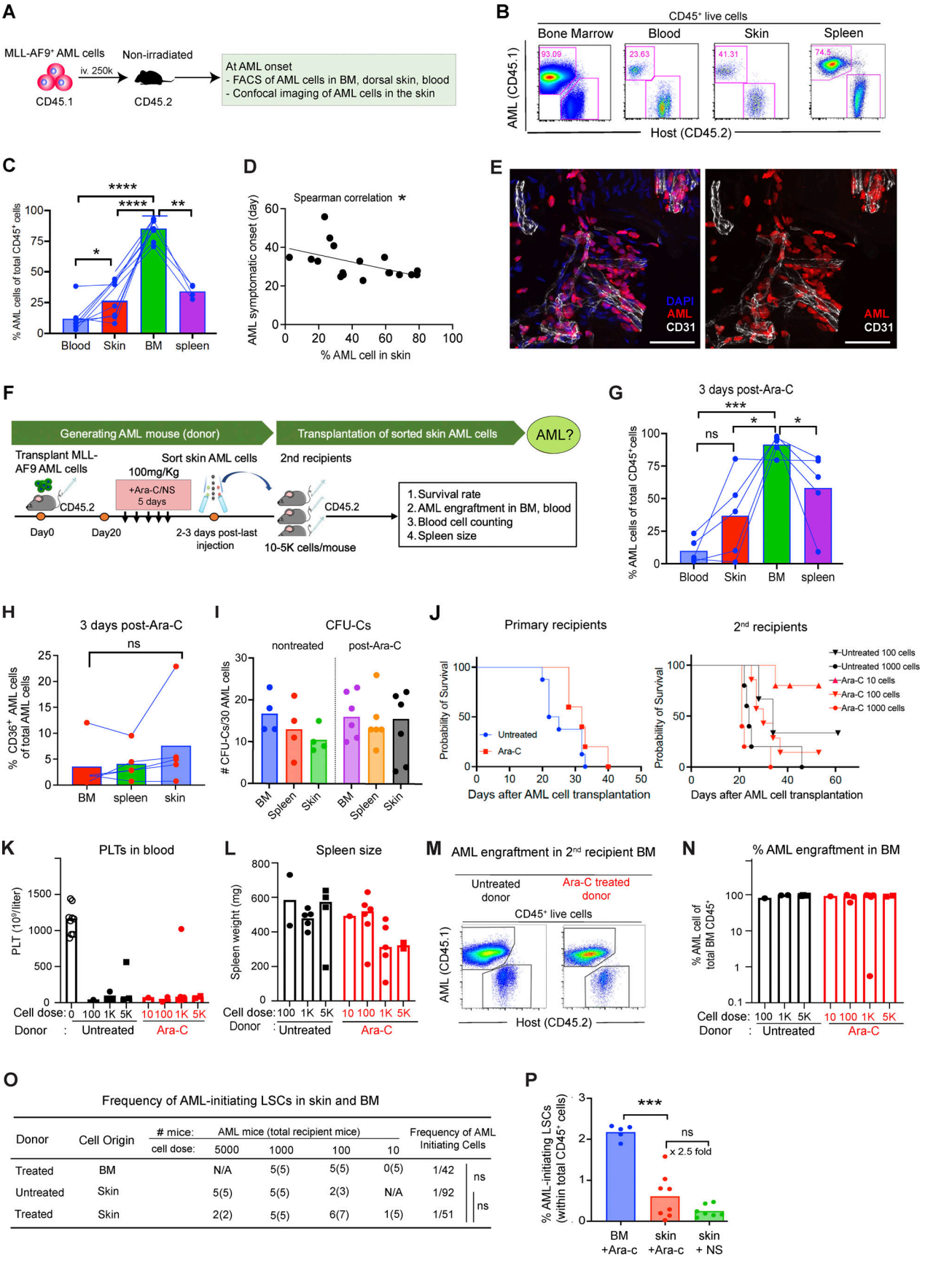

Donor	Cell Origin	# mice: / cell dose:	AML mice (total recipient mice) 5000	1000	100	10	Frequency of AML Initiating Cells	
Treated	BM		N/A	5(5)	5(5)	0(5)	1/42	ns
Untreated	Skin		5(5)	5(5)	2(3)	N/A	1/92	ns
Treated	Skin		2(2)	5(5)	6(7)	1(5)	1/51	

Figure 1. **AML cells infiltrated in skin are capable of regenerating AML after transplantation. (A)** Strategy to generate *MLL-AF9* AML mouse model. *MLL-AF9* transduced AML cells expressing CD45.1 were transplanted into non-irradiated CD45.2 C57BL/6 mice. **(B)** FACS profile showing AML engraftment analysis

in BM, PB, spleen, and dorsal skin at the end stage of AML. The numbers in the panel are the mean frequencies. **(C)** Proportion of the AML cells within total hematopoietic ($CD45^+$) cells in blood, skin, BM, and spleen. Data were from two independent experiments and each dot represents data from one mouse. The horizontal bars represent mean values. n = 4–9 per group, *P < 0.05, **P < 0.01, ****P < 0.0001, determined by paired t test, except the comparison between skin and blood where unequal number of mice were included. **(D)** The inverse correlation between AML engraftment in the skin with symptomatic AML onset. *P < 0.05, determined by Spearman correlation. Each dot represents data from a single recipient mouse, n = 18 mice. **(E)** Confocal image showing distribution of *MLL-AF9*$^+$ AML cells expressing DsRed at perivascular sites in dorsal skin. The AML cells were injected after sublethal irradiation of the mice. The endothelial cells were marked by CD31 expression (white). Scale bars are 50 µm. **(F)** Experimental strategy to assess AML-initiating capacity of the AML cells infiltrated in mouse skin by serial transplantation. The primary recipient mice (CD45.2) that developed AML after AML cell (CD45.1) transplantation were treated with Ara-C (100 mg/Kg) or saline (NS, untreated) for 5 d. The residual $CD45.1^+$ AML cells from skin were sorted at 2–3 d after the last injection of Ara-C and transplanted into secondary non-irradiated recipient CD45.2 mice at doses of 10, 100, 1,000, and 5,000 (5K) cells/mouse. The AML development was monitored by FACS and hematology analyzer Sysmex. The mice were sacrificed when found moribund. **(G)** AML engraftment in blood, skin, BM, and spleen of the primary recipients under steady state and 3 d after Ara-C treatment. Each dot represents data from a single mouse. n = 5 per group, *P < 0.05, ***P < 0.001, determined by paired t test. **(H)** The fraction of $CD36^+$ AML cells in the skin, BM, and spleen. Each dot represents data from a single mouse. ns, no significant difference, determined by paired t test. **(I)** The frequency of CFU-Cs derived from the residual AML cells in skin, spleen, and BM. **(J)** The Kaplan–Meier survival curve of the primary and secondary recipient mice. The curve was generated by Log-rank (Mantel–Cox test). Each dot represents an endpoint when the mice were found dead or sacrificed because of being moribund. Data were from two independent experiments. n = 5–8 primary recipients treated with Ara-C (n = 5) or NS (untreated), n = 5–7 secondary recipients per group. **(K)** Platelet counts in PB of the secondary recipient mice at the endpoint. Each dot represents data from a single mouse. **(L)** Spleen size of the secondary recipient mice at the endpoint. Each dot represents data from a single mouse. **(M)** FACS profile showing the engraftment of skin-derived AML $CD45.1^+$ cells in BM of the secondary recipient mice. **(N)** AML engraftment of the skin-derived AML $CD45.1^+$ cells in BM of the secondary recipient mice. Each dot represents data from a single mouse. **(O)** The frequencies of the secondary recipient mice that developed AML after injection of skin-derived AML cells. The frequency of AML-initiating LSCs was determined by extreme limiting dilution analysis (Hu and Smyth, 2009) based on the number of mice that developed AML after secondary transplantation. ns, no significant difference, determined by *Chi* square test. **(P)** The percentage of AML-initiating LSCs in BM and skin. The percentages were calculated based on the frequencies of AML-initiating LSCs determined by transplantation and shown in G and the percent AML cells within total $CD45^+$ mononuclear cells in each tissue. Each dot represents data from a single mouse. n = 5–8 per group, ns, no significant difference, ***P < 0.001, determined by unpaired t test. See also in Fig. S1.

failed to differentiate into chondrocytes in either monolayer or micromass pellet culture in which condition BM MSCs could differentiate into chondrocytes (Fig. S2 E). These data indicate that the $Ebf2^+$ and $Ebf2^-$PαS cells in mouse skin may represent bipotential MPCs although they have the same immunophenotype as BM MSCs.

Single-cell assay confirms osteo-adipo bipotentials of skin $Ebf2^+$ and $Ebf2^-$PαS cells

To validate the identity of the skin stromal subsets, we characterized these cells at a single-cell level. The limiting dilution experiment revealed that the CFU-F frequency in both skin $Ebf2^+$ and $Ebf2^-$PαS fractions was as high as 1 in 4 (Fig. 2, G and I). Of 13 randomly selected CFU-Fs from single $Ebf2^+$ cells, nine (69.2%) showed both osteogenic and adipogenic differentiation potency, although to different degrees (Fig. 2, H and K). However, only 45.4% (5 of 11) of the $Ebf2^-$PαS cells showed bilineage potency toward osteoblasts and adipocytes (Fig. 2, J and K). The chondrogenic potency, however, was not evaluated at single-cell level since none of these cell subsets differentiated into chondrocytes at the bulk level. The self-renewal capacity of the $Ebf2^+$ and $Ebf2^-$ cells was evaluated by serial replating of single CFU-F derived from the single sorted cells. 11 out of 25 CFU-Fs initially generated by single $Ebf2^+$ cells could be serially replated for beyond 10 passages (Fig. 2 L). Meanwhile, only 4 in 20 CFU-F clones derived from $Ebf2^-$PαS cells could be serially replated for over 10 passages (Fig. 2 L), indicating a limited self-renewal capacity of the $Ebf2^-$PαS cells. These data further support the notion that the skin $Ebf2^+$ and $Ebf2^-$PαS cells are enriched with osteo-adipogenic MPCs.

Skin $Ebf2^+$ cells are mainly located at perivascular sites

Similar to that in mouse BM, the skin $Ebf2^+$ cells did not express endothelial cell marker CD31 (Fig. S3 A). However, the $Ebf2^+$ cells highly expressed PDGFRb/CD140b, a marker expressed in pericytes (Armulik et al., 2011) and niche-forming perivascular cells in BM (Kusumbe et al., 2016; Fig. S3 B), pointing to a pericyte phenotype. Confocal imaging illustrated that the majority of the $Ebf2^+$ cells were adjacent to the endothelial cells in the skin (Fig. 3, A and B; and Fig. S3 C). Some scattered $Ebf2^+$ cells were also found in dermal panniculus carnosus, a layer of striated muscle (Fig. 3 A). Approximately 55 and 41% of the $Ebf2^+$ cells were positive for the pericyte marker NG2, respectively (Fig. S3, D and F), and 81% of them expressed α-smooth muscle actin (SMA; Fig. S3, E and F), reported to mark pericytes in BM (Baryawno et al., 2019). Altogether, these data suggest a perivascular origin and heterogeneity of the skin $Ebf2^+$ cells.

The $Ebf2^+$ cells in skin contribute to the mesenchymal cell turnover

To understand how mesenchymal cell niche in the skin is maintained, we determined the physiological contribution of the $Ebf2^+$ stromal cells to the niche formation by lineage tracing using Tg*Ebf2-Egfp* X Cre^{ERT2} X *Rosa26-tomato* mice (Fig. 3 C). This mouse model allowed us to track the fates of the $Ebf2^+$ cells in vivo since the $Ebf2^+$ cells express GFP and their progeny is marked by Tomato after tamoxifen (TAM) injection. About 15% of total $Ebf2^+$ cells were $Tomato^+$ ($Ebf2^+Tomato^+$) cells at 3 mo after TAM induction (Fig. S4, A and B). The $Ebf2^+Tomato^+$ cells could generate $Ebf2^-$PαS MPCs and more mature $CD45^-TER119^-CD31^-CD44^-CD140a^+SCA1^-$ stromal cells (Fig. 3, D and E), indicating the important role of the $Ebf2^+$ cells in maintaining the mesenchymal cell compartment in the skin.

The fraction of the $Ebf2^+Tomato^+$ cells within stromal cells remained constant up to 12 mo after TAM induction (Fig. 3 E), which is likely attributed to their self-renewal ability. However, the $Ebf2^-Tomato^+$ cells which were produced by the $Ebf2^+Tomato^+$ cells increased from 11% at 3 mo to 21% at 6 mo after TAM injection

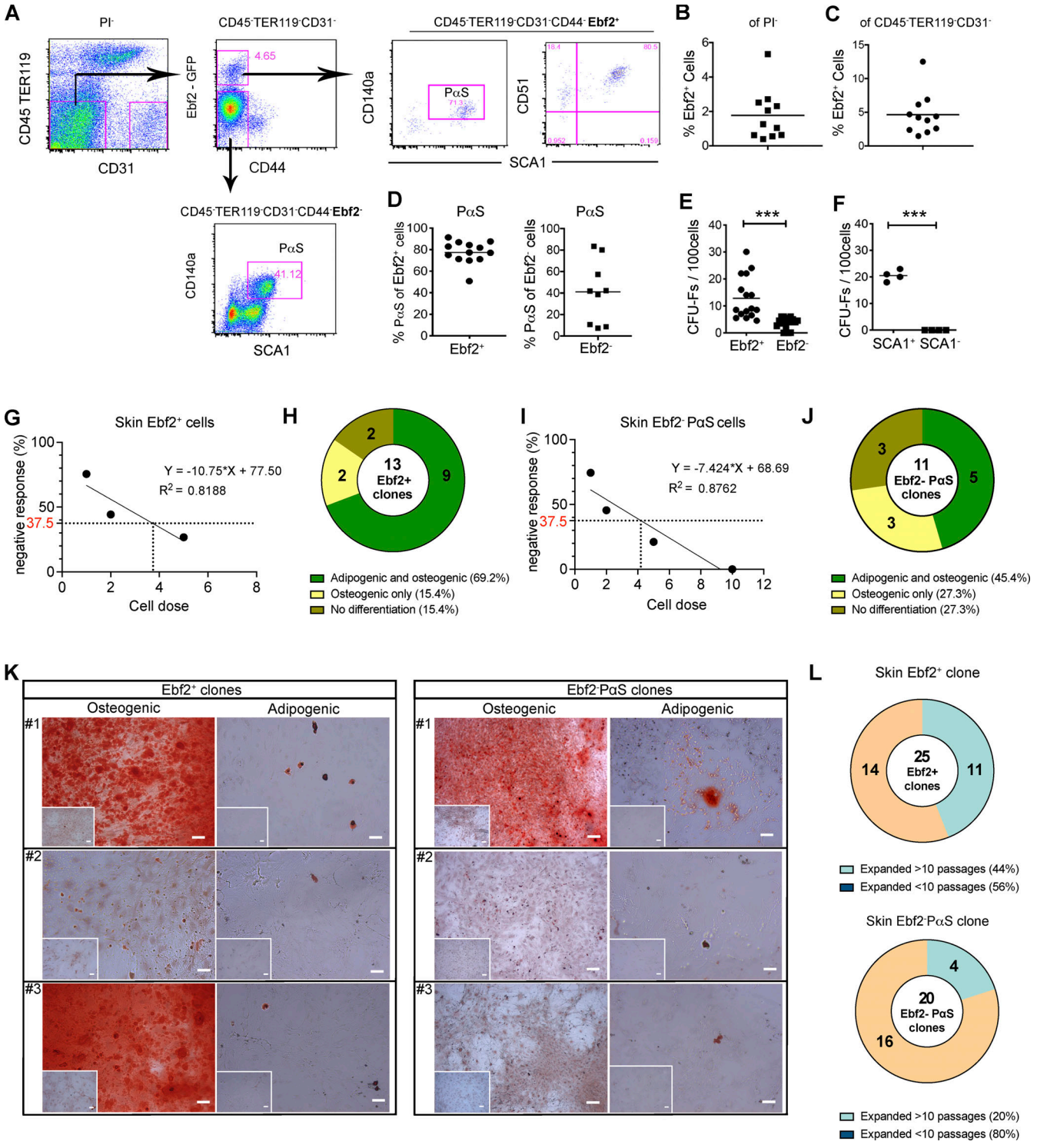

Figure 2. **Identification of skin MPC subsets by Ebf2 expression. (A)** A representative FACS profile showing FACS sorting/analysis of the Ebf2⁺ and Ebf2⁻ cells in dorsal skin. The cells were first gated within non-hematopoietic (CD45⁻TER119⁻) and non-endothelial (CD31⁻) live (PI⁻) stromal cells. These cells lacking expression of CD44 were further analyzed for their expression of SCA1, PDGFRa/CD140a (PαS), and CD51. The numbers in the panel are the mean frequencies. **(B and C)** The Ebf2⁺ cell frequency within total PI⁻ (B) or PI⁻CD45⁻TER119⁻CD31⁻ stromal cells (C) in dorsal skin. **(D)** The fractions of PαS cells within the Ebf2⁺ and Ebf2⁻ stromal cells. Each dot in B–D represents data from a single mouse in three to six experiments with the horizontal line as a mean value. **(E)** CFU-Fs in the Ebf2⁺ and Ebf2⁻ stromal cells. **(F)** CFU-Fs were exclusively found in the Ebf2⁺SCA1⁺ cell fraction. Data in E and F are from three independent experiments and each dot represents replicate assays from two to three mice in each experiment. The horizontal line represents mean value. ***P < 0.001, determined by Wilcoxon matched-signed pair rank test. **(G–J)** Single-cell analysis of CFU-Fs and lineage differentiation from the FACS-sorted Ebf2⁺ (G and H) and Ebf2⁻PαS (I and J) stromal cells. The CFU-F frequencies (G and I) were determined by limiting dilution at a density of 1, 2, 5, and 10 cells per well in a 96-well plate and the frequency of the single cells with bilineage plasticity (H and J) were assessed by multilineage differentiation potential of single CFU-Fs derived from the cells. The simple linear regression was used to determine the dose responses in G and I. **(K)** Representative images of the osteogenic and adipogenic differentiation from single CFU-F clones

derived from Ebf2⁺ and Ebf2⁻PαS cells. Scale bars in the images for Ebf2⁺ cells are 100, and 250 and 100 µm in the images for osteogenic and adipogenic differentiation from Ebf2⁻PαS cells. **(L)** PDT of randomly selected CFU-Fs derived from single Ebf2⁺ and Ebf2⁻PαS cells. Each line represents the growth kinetics of a single clone. See also in Fig. S2.

and then remained stable (Fig. 3 E). Within the newly generated Ebf2⁻Tomato⁺ cells, the majority were PαS MPCs and about 5% were the CD140a⁺SCA1⁻ cells (Fig. 3 F). Inversely, within the total PαS MPCs, only 0.5% were Ebf2⁺Tomato⁺ cells and 30% were the newly generated Ebf2⁻Tomato⁺ PαS cells at 6 mo after TAM (Fig. S4, C–E). These data suggest a substantial contribution of the Ebf2⁺ MPCs to generating the Ebf2⁻Tomato⁺PαS MPCs while maintaining the Ebf2⁺ cell pool.

Similar to the Ebf2⁺ cells, the Ebf2⁻Tomato⁺ cells were mainly distributed in the lower dermis and adjacent to CD31⁺ endothelial cells (Fig. 3 G). However, they lacked NG2 expression (Fig. S4 F). Only 19% and 28% of the Ebf2⁻Tomato⁺ cells expressed NESTIN and α-SMA, respectively (Fig. S4, G–I).

Altogether, skin harbors Ebf2⁺ and Ebf2⁻PαS MPCs with a similar phenotype as BM MSCs. The Ebf2⁺ MPCs reside at the top of the developmental hierarchy and contribute to mesenchymal cell generation in the skin.

Skin MPCs play a role in maintaining normal hematopoietic and AML cells in vitro

Identification of the skin MPC populations made it possible to analyze their potential role in the maintenance of AML cells. We first evaluated the function of skin MPC subsets in supporting normal hematopoietic stem cells (HSCs) in a coculture system and compared it with BM MSCs (Fig. S5 A). Similar to their BM counterparts, both skin Ebf2⁺ and Ebf2⁻PαS MPCs were able to maintain HSC activities, indicated by similar numbers of CFU-Cs generated from the Lineage⁻ SCA1⁺KIT⁺(LSK) CD150⁺ cells after the coculture with skin MPCs or BM MSCs (Fig. S5, B and C). Further, similar cobblestone area-forming cells (CAFCs) were generated from the BM LSK cells cocultured with the skin MPCs or BM MSCs (Fig. S5, D and E). The BM Ebf2⁻PαS cells displayed better capacity in supporting CAFC formation from the LSK cells than the BM Ebf2⁺ MSCs (Fig. S5 F). Altogether, these data indicated that skin MPCs possessed similar hematopoiesis supportive function as BM MSCs.

To assess the role of skin MPCs in supporting AML LSC growth, we next performed CAFC assay of *MLL-AF9*⁺ AML cells (Fig. 4 A). Like BM MSCs, skin MPC subsets could support CAFC formation from the AML cells, but to a lesser degree than the BM Ebf2⁻PαS cells (Fig. 4, B and C).

Increasing evidence suggests that BM stromal cells may protect leukemia cells from cytostatic drugs (Alonso et al., 2015; Iwamoto et al., 2007; Jin et al., 2008; Xu et al., 2016; Zhang et al., 2013). However, it is not known if extramedullary stromal cells have similar functions. We then tested the chemoprotective function of skin MPCs by CAFC assay. We administered Ara-C 2 d after seeding the *MLL-AF9*⁺ AML cells to the MPCs to allow for efficient cell–cell interactions (Fig. 4 A). Both skin Ebf2⁺ and Ebf2⁻PαS cells could protect the AML LSCs from Ara-C treatment, demonstrated by the persistence of residual CAFCs after Ara-C treatment, in striking contrast to the efficient killing of the AML cells cultured alone (Fig. 4, D and E). No difference in the frequency of KIT⁺ AML cells representing AML LSCs (Somervaille and Cleary, 2006) was observed among all the cocultures (Fig. 4 F). However, the numbers of the residual KIT⁺ LSCs were significantly increased in the cocultures with the stromal cells compared with the monoculture after Ara-C treatment (Fig. 4 G). CD36 was reported to be a marker for chemoresistant leukemic cells (Farge et al., 2017; Landberg et al., 2018; Ye et al., 2016). After Ara-C, the CD36⁺ AML cells were selectively enriched in all the cocultures except that with skin Ebf2⁻PαS MPCs (Fig. 4 H); however, only in the culture with skin MPC subsets, significantly more CD36⁺ AML cells were retained (Fig. 4 I). These data indicate a previously unrecognized role of skin MPCs in AML LSC maintenance and protection.

The altered mesenchymal niches in the skin during AML development

Niche remodeling in BM has been considered one of the mechanisms contributing to leukemia progression (Åhsberg et al., 2020; Cai et al., 2022; Duarte et al., 2018; Xiao et al., 2018b). By confocal imaging, we observed the perivascular location of the AML cells (Fig. 1 E) and the localization adjacent to the skin Ebf2/GFP⁺ MPCs (Fig. 4 J). We then evaluated whether the skin cellular niches were remodeled by the AML cells. The proportion of Ebf2⁺ MPCs but not the Ebf2⁻PαS cells in the skin stromal cells were reduced after symptomatic onset of AML (Fig. 4, K–N). While this finding seems to be contrary to our previous observation of BM MSC increase in AML mouse BM, it is somewhat consistent with the reduced PαS cell fraction within the Ebf2⁺ cells in the AML mouse BM (Xiao et al., 2018b). In addition, while the total CD31⁺ endothelial cells were unaltered, as observed in BM (Xiao et al., 2018b), the CD31⁺SCA1⁺ arteriolar endothelial cells were significantly increased (Fig. 4, O and P), indicating an increase of arterioles in dorsal skin during AML development.

Molecular evidence for the role of skin MPCs in hematopoiesis and AML

To investigate the molecular mechanisms behind the hematopoiesis-supportive function of the skin MPCs, we performed RNA sequencing on the freshly sorted skin Ebf2⁺ and Ebf2⁻PαS MPCs. This revealed a distinct transcriptional profile of skin MPCs and BM MSCs with 1,150 and 816 genes differentially expressed between skin Ebf2⁺ and Ebf2⁻PαS MPCs compared with BM MSCs, respectively (Fig. 5 A). However, only 135 genes were differentially expressed between the skin Ebf2⁺ and Ebf2⁻PαS cells. Among them, the genes associated with TNFα signaling, angiogenesis, and epithelial-to-mesenchymal transition were upregulated, while the cell proliferation genes were downregulated in the more primitive Ebf2⁺ cells (Fig. 5 B). We then compared skin MPC pool (Ebf2⁺ and Ebf2⁻PαS) with BM MSCs. The genes related to skin tissue maintenance (*Krt14*, *Krt19*)

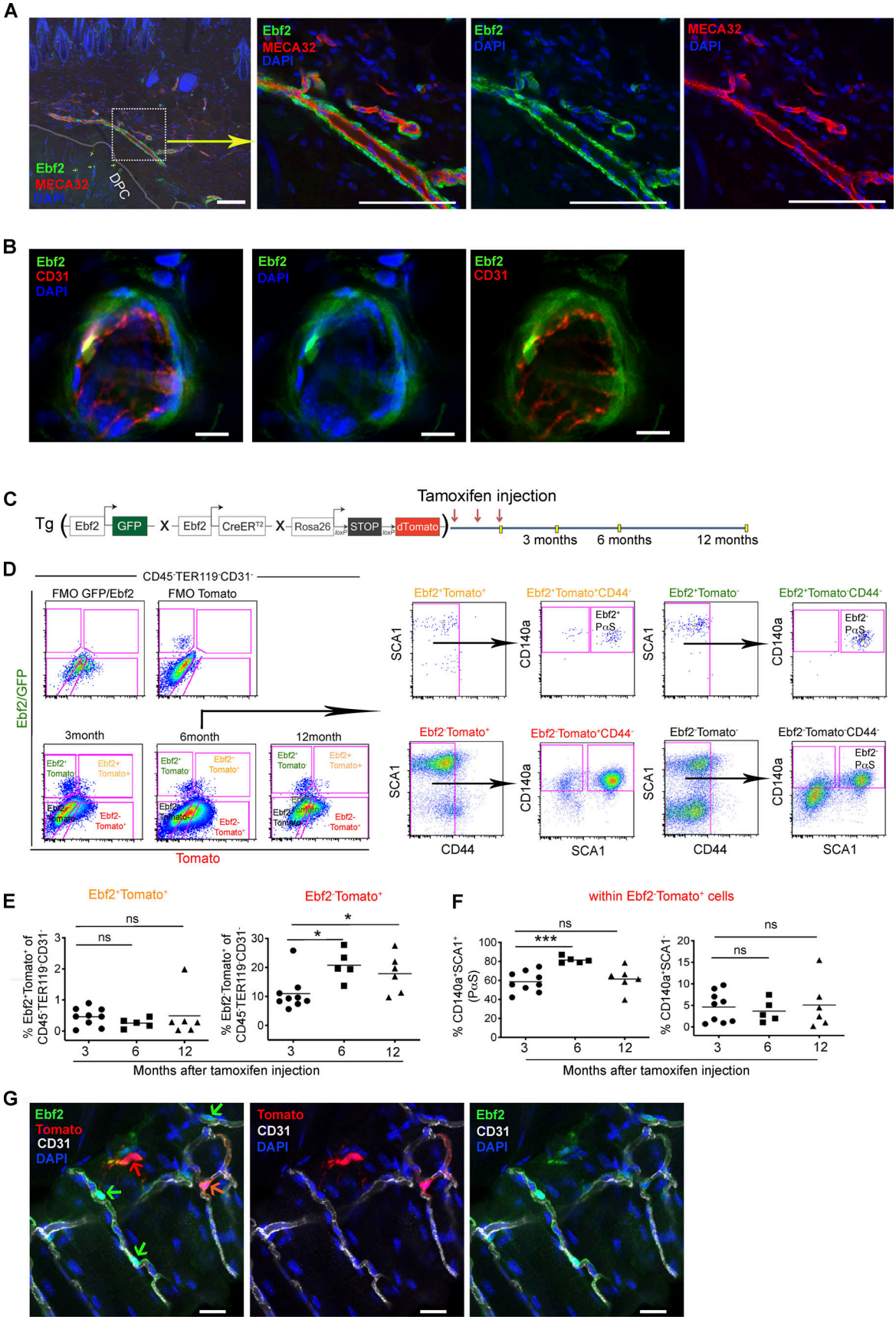

Figure 3. **Distribution and hierarchical relationship of skin MPCs. (A)** Localization of Ebf2+ cells in skin perivascular area and dermal panniculus carnosus (DPC). The endothelial cells in the vessels were identified by MECA32 staining. Arrows point to the Ebf2+ cells in the DPC area. Scale bars are 100 µm.

(B) Representative image showing the perivascular localization of Ebf2$^+$ cells adjacent to CD31$^+$ endothelial cells in dorsal skin. Scale bars are 10 µm. **(C)** A scheme showing strategy for lineage tracing of the Ebf2$^+$ cells in skin. The Ebf2/GFP$^+$Tomato$^+$ cells and their progenies (Ebf2/GFP$^-$Tomato$^+$) were traced by FACS at 3, 6, 12 mo after TAM injection. **(D)** A representative FACS profile showing analysis of activated Ebf2$^+$ cells (GFP$^+$Tomato$^+$) and their progeny (GFP$^-$Tomato$^+$). The gates for different cell subsets were defined with FMO from bitransgenic or single-transgenic mice. Each stromal cell subset (PI$^-$CD45$^-$TER119$^-$CD31$^-$) was gated within the CD44$^-$ fractions and subsequently gated for PαS cells based on CD140a and SCA1 expression. **(E)** The frequencies of Ebf2/GFP$^+$Tomato$^+$ cells and its progenies (Ebf2/GFP$^-$Tomato$^+$) within stromal cells. Each dot represents data from each mouse from two to three independent experiments. Horizontal bars represent the mean, *P < 0.05, determined by unpaired *t* test. **(F)** The fractions of PαS and Ebf2$^-$CD140a$^+$SCA1$^-$ cells within total GFP$^-$Tomato$^+$ cells generated by Ebf2$^+$ cells. Each dot represents data from each mouse from two to three independent experiments. Horizontal bars represent the mean, ***P < 0.001, determined by unpaired *t* test. **(G)** Distribution of the single Ebf2/GFP$^+$Tomato$^-$ cells (green arrows), activated Ebf2/GFP$^+$Tomato$^+$ cells (orange arrows), and Ebf2/GFP$^-$Tomato$^+$ (red arrows) cells at 3 mo after TAM injection. Scale bars are 20 µm. See also in Figs. S3 and S4.

and adipogenesis (*Fabp4*) were upregulated in the skin MPCs (Fig. 5, C and D), showing tissue origin-related characteristics of these cells. Consistent with the limited chondrogenic differentiation capacity of skin MPCs (Fig. S2, C and D), the genes associated with chondrogenesis were downregulated in the cells (Fig. 5 E). Conversely, skin MPCs were enriched with genes related to fatty acid metabolism and oxidative phosphorylation, indicating a distinct metabolic profile between the skin and BM MSCs (Fig. 5, D and E). Furthermore, the genes related to inflammatory response were enriched in the skin MPCs relative to BM MSCs (Fig. 5, E and F), indicating a possible proinflammatory phenotype of skin MPCs.

Notably, there was no overall significant difference in the hematopoiesis supportive gene expression between the skin MPCs and BM MSCs (Fig. 5 G). The findings were confirmed by qPCR of the genes in these freshly sorted cells (Fig. 5 H). Similar to BM MSCs, both skin MPC subsets expressed *Cxcl12*, *Kitl*, *Jag1*, *Lama4*, and *Angptl1*, all of which are known to be critical for hematopoiesis maintenance and regeneration (Arai et al., 2004; Calvi et al., 2003; Greenbaum et al., 2013; Gu et al., 2003; Omatsu et al., 2010; Poulos et al., 2013; Susek et al., 2018; Thorén et al., 2008). The expressions of *Kitl*, *Jag1*, and *Lama4* were even significantly higher in skin Ebf2$^+$ and Ebf2$^-$PαS cells than that in BM MSCs. Moreover, the expression of *Spp1*, a negative regulator of HSC expansion (Stier et al., 2005), was lower in skin MPCs than that in BM MSCs (Fig. 5, C and H). These data provide molecular evidence for the supportive function of skin MPCs for HSCs and AML LSCs.

Enhanced mitochondrial transfer from skin MPCs to AML cells associated with increased chemoprotection of AML cells

To reveal the mechanisms underlying the function of skin MPCs in maintaining and protecting AML LSCs, we examined the metabolic activity of skin MPCs in supporting AML cells since the genes related to oxidative phosphorylation and fatty acid metabolism are enriched in the skin MPCs. Mitochondrial transfer has been reported as one of the protective mechanisms during chemotherapy in leukemias by providing energy support and antioxidant machinery to counteract oxidative stress induced by chemotherapy (Batsivari et al., 2020; Cai et al., 2022; Marlein et al., 2017; Moschoi et al., 2016). Consistent with their gene expression profile, our FACS analysis showed increased mitochondrial mass of skin MPCs compared with BM MSCs (Fig. 6, A and B). Further, in a coculture with mitochondria-prelabeled skin MPCs (Fig. 6 C), we detected enhanced mitochondrial transfer from skin MPCs to the AML cells compared with BM MSCs (Fig. 6, D and E). Correspondingly, the AML cells cocultured with skin MPCs showed lower ROS levels and higher viability during Ara-C treatment (Fig. 6, F and G). The mitochondrial transfer and chemoprotection could be partially reversed by the treatment with microtubule inhibitor nocodazole and colchicine in the cocultures (Fig. 6, H–J). Similar to a previous report (Moschoi et al., 2016), the mitochondrial transfer seemed to be leukemia-specific since little or no mitochondrial transfer from skin MPCs to normal HSPCs (LSK BM cells) was detected in the cocultures (Fig. 6, K and L). Together, these data indicated that skin MPCs could maintain AML LSCs and protect them from Ara-C treatment in vitro partially by reducing oxidative stress.

Lama4 loss in skin MPCs enhanced AML LSC proliferation and chemoprotection in vitro

Lama4 was highly expressed in skin MPCs (Fig. 5 H), and we have found that *Lama4* loss in mice promoted AML LSC proliferation, chemoresistance, and relapse (Cai et al., 2022). This has tempted us to test the impact of *Lama4* deletion in skin MPCs on AML LSC growth (Fig. 6 M). We observed increased AML cell proliferation and chemoresistance to Ara-C at 24 h after coculture with *Lama4*$^{-/-}$ skin MPCs (Fig. 6 N). Further CAFC assay indicated that *Lama4*$^{-/-}$ skin MPCs promoted AML LSC proliferation and chemoresistance to Ara-C (Fig. 6 O), suggesting a suppressive impact of *Lama4* expression in skin MPCs on AML cell growth and chemoresistance.

The increased chemoresistant AML cells in *Lama4*$^{-/-}$ mouse skin after Ara-C treatment

To further explore the molecular mechanism involving the role of the extramedullary niche in the skin for maintaining residual AML cells after chemotherapy, we here took advantage of *Lama4*$^{-/-}$ mice where AML progression and relapse are accelerated (Cai et al., 2022). To facilitate imaging of engrafted AML cells, DsRed-expressing *MLL-AF9* AML cells were transplanted in sublethally irradiated *Lama4*$^{+/+}$ and *Lama4*$^{-/-}$ mice (Fig. 7 A). The mice were treated with either Ara-C or NS for 5 d on day 15 after AML transplantation. Interestingly, 1 d after Ara-C treatment, confocal imaging illustrated more AML cells in *Lama4*$^{-/-}$ mouse skin compared with that in *Lama4*$^{+/+}$ mice following either NS or Ara-C treatment (Fig. 7 B). However, such a difference was not detected by FACS while there was a clear reduction of the AML cells in the peripheral blood (PB) and skin after Ara-C treatment (Fig. 7 C). It is possible that some of the remaining AML cells were lost during enzymatic digestion of the skin for FACS

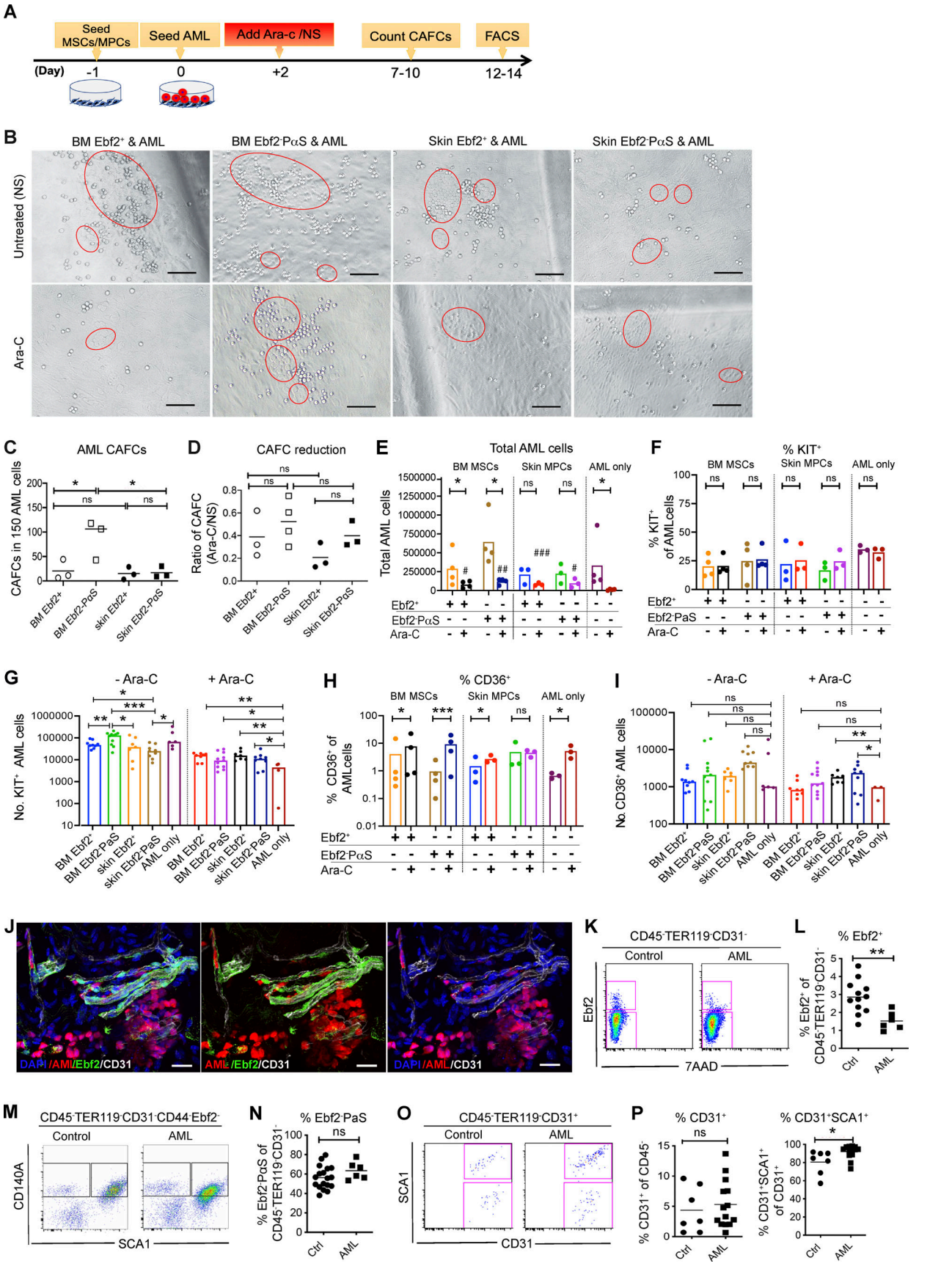

Figure 4. **Skin MPCs support AML LSC growth and protect them from chemotherapy. (A)** Experimental strategy for assessing the role of the skin MPC and BM MSC subsets for AML growth by CAFC assay. **(B)** Representative images of CAFCs derived from the AML cells. Scale bars are 100 µm. **(C)** Total

numbers of CAFCs generated from 150 *MLL-AF9*$^+$ AML cells. **(D)** A proportion of residual CAFCs from AML cells after Ara-C treatment relative to the NS-treated controls. **(E)** The total number of the AML cells at 10 d after Ara-C treatment. **(F and G)** The frequency (F) and the numbers (G) of the KIT$^+$ AML LSCs. **(H and I)** The frequency (H) and the numbers (I) of the CD36$^+$ chemoresistant AML cells. Data in C–I were from three to four independent experiments and each dot represents the mean of replicate assays. The horizontal bars represent mean values. *P < 0.05, **P < 0.01, ***P < 0.001, determined by unpaired (C, D, G, and I) or paired (E, F, and H) *t* test between Ara-C treated and nontreated cocultures within the same stromal cell type. #P < 0.05, ##P < 0.01, ###P < 0.001 determined by unpaired *t* test when comparing the Ara-C treated AML cells in cocultures with BM MSCs or skin MPCs with the Ara-C treated AML monoculture. **(J)** Colocalization of AML cells (red) with the Ebf2$^+$ cells. Ebf2 was determined by GFP (green) and the endothelial cells were marked by CD31 (white). Scale bars are 20 µm. **(K)** Representative FACS plot showing analysis of Ebf2$^+$ MPCs in AML mouse dorsal skin. **(L)** The frequency of the Ebf2$^+$ MPCs within stromal cells in dorsal skin tissue at end stage of AML. Data were from six independent experiments, and each dot represents data from one mouse. The horizontal bars represent mean values. **P < 0.01, determined by unpaired *t* test. **(M)** Representative FACS plot showing analysis of the skin Ebf2$^-$PαS MPCs in healthy controls and AML mice. **(N)** The frequency of the Ebf2$^-$PαS cells within stromal cells in dorsal skin at the end stage of AML. Data were from six independent experiments and each dot represents a mouse. The horizontal bars represent, mean values. ns, no significant difference, determined by unpaired *t* test. **(O)** FACS profile showing analysis of CD31$^+$ cells in the dorsal skin of healthy and AML mice. **(P)** The frequency of total endothelial cells (CD31$^+$) and arteriolar endothelial cells (CD31$^+$SCA1$^+$). ns, no significant difference, *P < 0.05, determined by Mann–Whitney test.

whereas confocal imaging was performed on the tissue fixed directly after dissecting. It is important to note that the chemoresistant CD36$^+$ AML cells (Farge et al., 2017; Ye et al., 2016), not KIT$^+$ cells, were enriched in *Lama4*$^{-/-}$ mouse skin after Ara-C treatment (Fig. 7 D), which was not observed in the BM (Cai et al., 2022). It is worth mentioning that there was no homing preference of the AML cells to *Lama4*$^{-/-}$ skin and BM compared with that in *Lama4*$^{+/+}$ mice (Fig. 7, E–G), suggesting that the observation of more AML cells in *Lama4*$^{-/-}$ mouse skin was not related to the initial homing of the AML cells. Further, the AML cell homing to skin and BM was similar at 3 h after transplantation (Fig. 7 H), pointing toward a possibility that the skin tissue may act as an independent AML niche from the BM.

To functionally evaluate AML-initiating LSCs, we performed serial transplantation with limited cell doses (10, 100, and 1,000 cells/mouse) and CFU-C assay after Ara-C treatment (Fig. 8 A). Extreme limiting dilution analysis (Hu and Smyth, 2009) indicated no significant difference in the frequency of AML-initiating LSCs within the residual AML cells from *Lama4*$^{+/+}$ and *Lama4*$^{-/-}$ mouse skin (Fig. 8, B and C). However, due to a relatively higher percentage of total AML cells in the donor *Lama4*$^{-/-}$ mouse skin than that in the *Lama4*$^{+/+}$ mice (Fig. 8 D), the calculated percentage of the AML-initiating LSCs and AML CFU-Cs in the *Lama4*$^{-/-}$ skin appeared to be higher than that in the *Lama4*$^{+/+}$ skin (Fig. 8 E). These data suggest that *Lama4* expression in skin mesenchymal niche plays a role in maintaining the chemosensitivity of AML cells in the skin to Ara-C.

Discussion

Leukemia cutis is commonly observed in patients with monocytic AML, and pediatric patients with congenital leukemia are prone to develop leukemia cutis (Parsi et al., 2020). Despite its association with a poor prognosis (Bakst et al., 2011; Gouache et al., 2018; Wang et al., 2019), the pathogenesis and impact of leukemia cutis on AML relapse remain largely unknown. We here have demonstrated in a transplantation-induced *MLL-AF9* AML mouse model that the AML cells infiltrate in mouse skin, similar to leukemia cutis observed in patients with AML. Importantly, these skin-derived AML cells can efficiently regenerate AML after transplantation even at a low dose (10 cells per mouse), indicating their high capacity in regenerating AML and pointing to a possible involvement of these leukemic cells in the relapse of AML.

Currently, little is known about the leukemia microenvironment or niche in the skin, which has limited our understanding of how leukemia cutis is maintained. We report that skin harbors two MPC subsets distinguished by Ebf2 expression, the Ebf2$^+$ and Ebf2$^-$PαS cells, sharing a similar phenotype with BM MSCs (Morikawa et al., 2009; Qian et al., 2013; Qian et al., 2012). The skin Ebf2$^+$ MPCs coexpress pericyte markers like CD140b/PDGFRb and α-SMA and show pericyte phenotype. The adjacent localization of the Ebf2$^+$ cells to the AML cells in skin indicated a possibility that these cells act as a niche component for maintaining AML cells. This notion is supported by another important finding in this study that skin MPCs, similar to BM MSCs, show a supportive/protective function for AML LSCs. During AML progression, the skin mesenchymal cell niches are also altered with increased arteriolar endothelial cells and reduced Ebf2$^+$, but not Ebf2$^-$PαS MPCs, after symptomatic AML onset. The niche remodeling might in turn further promote AML progression since Ebf2$^+$ cell deletion in mice accelerated AML development, as reported (Xiao et al., 2018b).

We have here attempted to address the potential mechanisms mediating the supportive role of skin MPCs. It is most likely that multiple mechanisms are involved in the AML protective role of skin MPCs. Mitochondrial transfer from stromal cells to leukemic cells has been reported to be one of the mechanisms to protect leukemic cells to survive chemotherapy by providing an antioxidant system to counteract the therapy-induced oxidative stress (Forte et al., 2020). We find an increased mitochondrial mass in skin MPCs and enhanced mitochondrial transfer from skin MPCs to the AML cells during chemotherapy compared with that in BM MSCs. Blocking mitochondrial transfer by microtubule inhibitors in the coculture could compromise the protective effects of skin MPCs. These data suggest that skin MPCs may protect the AML cells by providing metabolic support via mitochondrial transfer. This notion was further supported by the enrichment of genes related to oxidative phosphorylation, fatty acid metabolism, and glycolysis in skin MPCs. Furthermore, the skin MPCs express a higher level of *Lama4*, *Kitl*, and *Jag1* than BM MSCs, which are known to be important for normal hematopoiesis maintenance and leukemic cell proliferation (Cai et al., 2022; Poulos et al., 2013; Somervaille and Cleary, 2006; Thorén et al., 2008). Our data indicate that *Lama4* expression in skin MPCs may have an impact on AML LSC

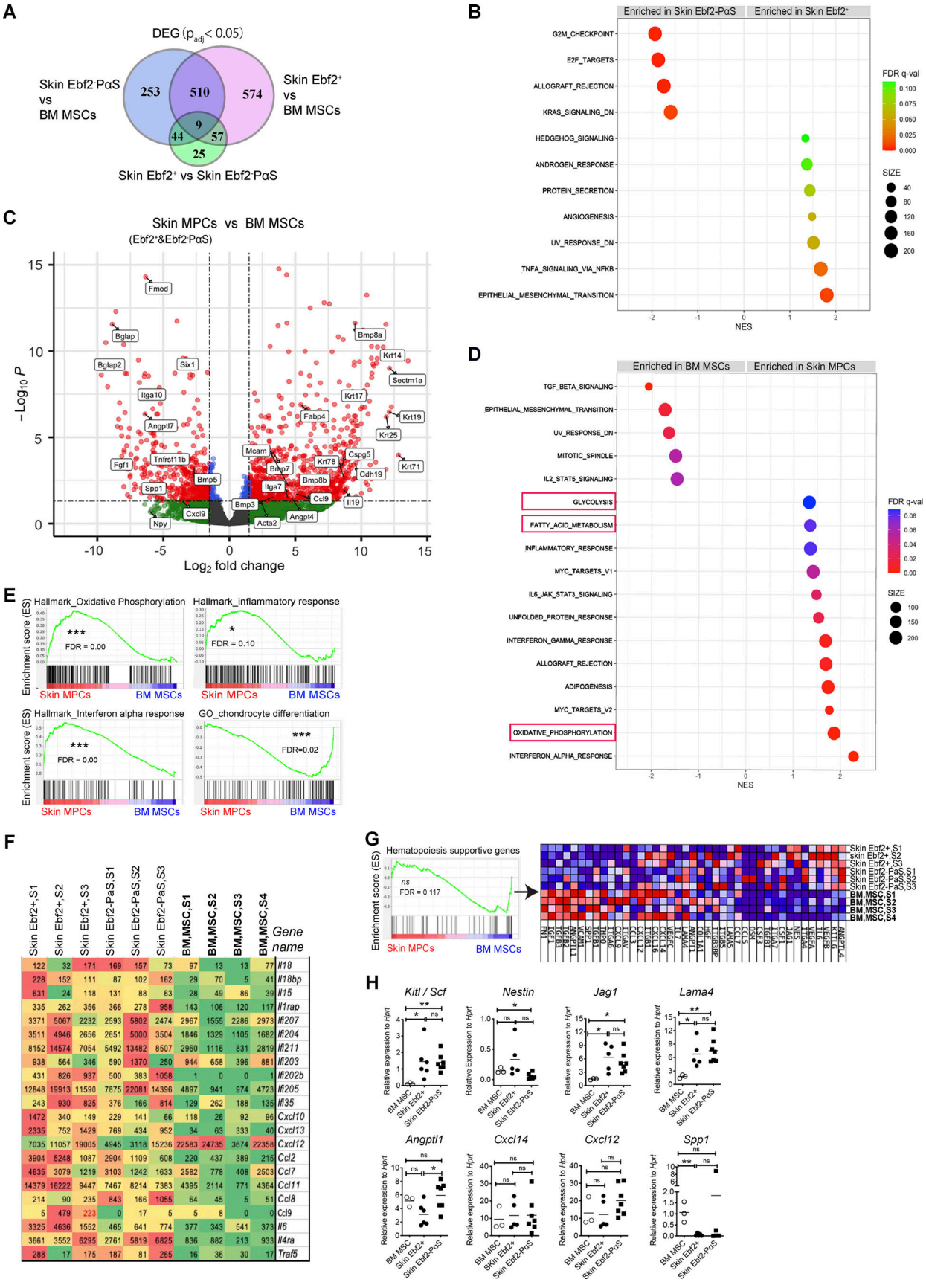

Figure 5. **RNA sequencing revealed the molecular profile of skin Ebf2⁺ and Ebf2⁻PαS MPCs. (A)** Venn diagram showing differentially expressed genes (DEG) among the skin Ebf2⁺ MPCs, skin Ebf2⁻PαS MPCs, and BM MSCs. **(B)** GSEA revealed the enrichment of genes associated with different biological

processes and cellular responses in the skin Ebf2⁺ and Ebf2⁻PαS MPC subsets. **(C)** A volcano plot showing differentially expressed genes between skin MPCs (Ebf2⁺ and Ebf2⁻PαS) and BM MSCs. **(D)** GSEA revealed the enrichment of gene sets associated with various biological processes and cellular responses in the skin MPCs (Ebf2⁺ and Ebf2⁻PαS) and BM MSCs. **(E)** GSEA plots showing the enrichment of genes related to oxidative phosphorylation, inflammatory, interferon α response, and chondrocyte differentiation in the skin MPCs compared to that in BM MSCs. FDR, false discovery rate. *P < 0.05, ***P < 0.001, determined by GSEA software. **(F)** Heatmap showing the expressions of selected inflammatory cytokines in skin Ebf2⁺ cells, Ebf2⁻PαS cells, and BM MSCs. The heatmap was created in Excel using conditional formatting. The color scale was set based on the minimum, midpoint, and maximum values of each gene in each row. Red correlates with high expression and green correlates with low expression. **(G)** Gene set enrichment plot showing hematopoiesis supportive niche genes in skin MPC subsets and BM MSCs, and the heatmap showing the gene expression levels. ns, no significant difference, determined by GSEA software. **(H)** qPCR of HSC niche genes in BM MSCs and skin Ebf2⁺ and Ebf2⁻PαS MPCs. Each dot represents mean of triplicate measurement of the gene expression relative to *Hprt*. Horizontal bars represent the mean values. Data were from three independent sorting experiments. ns, no significant difference, *P < 0.05, **P < 0.01, determined by unpaired *t* test.

chemosensitivity since *Lama4* deletion in skin MPCs led to enhanced proliferation and chemoprotection of AML LSCs. More work is required for assessing the potential impact of other niche factors like *Kitl*, *Jag1*, and *Angptl1*. In addition, the upregulation of inflammatory cytokines including interferon, *Il6*, *Il18*, *Il4*, and *Cxcl10* in the skin MPCs points to another possible mechanism contributing to the AML maintenance in the skin, as these cytokines affect leukemic/cancer cell growth (Madapura et al., 2017; Manshouri et al., 2011; Peña-Martínez et al., 2018; Welner et al., 2015).

The origin of the AML cells in the skin remains an open question. In patients, leukemia cutis is usually present concurrently with AML cell infiltration in BM. However, in some cases, it may precede systemic involvement (Krooks and Weatherall, 2018). Therefore, it is unclear whether the leukemic cells infiltrated in the skin originate from BM. We here find that the AML engraftment in the skin does not correlate with that in the blood, suggesting AML cell maintenance in the skin may not be dependent on the circulating AML cells although they were initially derived from the injected AML cells. On the contrary, the AML burden in skin inversely correlates with the time of AML symptomatic onset, which is in line with the association of leukemia cutis with poor prognosis in patients with AML (Krooks and Weatherall, 2018).

In summary, we here report that skin harbors primitive Ebf2⁺ MPCs and the downstream Ebf2⁻ MPCs. These MPCs are colocalized with AML cells at perivascular sites during AML development. The residual AML cells in the skin after chemotherapy can regenerate leukemia after transplantation, indicating the existence of AML LSCs in the skin. The skin MPCs can provide metabolic support for AML cells to protect them from chemotherapy in vitro. We for the first time provide evidence for the characteristics of skin mesenchymal cell niches and their roles in AML LSC growth and chemotherapy response, as well as the impact of *Lama4* expression in the niches on the chemoprotection of AML LSCs. These findings warrant future studies on the role of skin mesenchymal niches in chemotherapy response and relapse of AML patients.

Materials and methods

Mice

Ebf2-Egfp reporter FVB/N mice (RRID:MGI:4421814; Qian et al., 2013) 8–14 wk old were used. Transgenic *Ebf2-Egfp* X *Ebf2-Cre^{ERT2}* X *Rosa26^{loxp}Stop^{loxp}-Tomato* mice were generated by crossing *Ebf2-Egfp* with *Ebf2-Cre^{ERT2}* X *Rosa26^{loxp}Stop^{loxp}-Tomato* mice for lineage tracing. To activate Cre, TAM (Sigma-Aldrich) was intraperitoneally injected at 3 mg/20 g body weight three times every second day (Xiao et al., 2018b). *Lama4$^{-/-}$* C57BL/6 mice were generated as described (Thyboll et al., 2002). All mice were maintained in specific-pathogen-free conditions in the animal facility of Karolinska Institute. Animal procedures were approved by the local ethics committee (ethical number 15861-2018) at Karolinska Institute (Stockholm, Sweden).

Generation of *MLL-AF9*–induced AML mouse model

AML mouse model was induced as previously described (Xiao et al., 2018b). Briefly, 250,000 *MLL-AF9* expressing cells were intravenously injected into non-irradiated mice to generate the AML mouse model. For detecting AML infiltration in dorsal skin tissue, 1 × 10^6 of *MLL-AF9* previously generated in DsRed C57BL/6J transgenic mice (Hartwell et al., 2013) were intravenously injected into sublethally irradiated (6 Gy) *Lama4$^{+/+}$* and *Lama4$^{-/-}$* mice, as described (Cai et al., 2022). On day 15, the mice were treated intraperitoneally with Ara-C (Jena Bioscience) at a dose of 100 or 700 mg/kg body weight, daily for five consecutive days. For non-irradiated mice, the treatment started on day 20. The mice were sacrificed 1 d after the last injection for AML engraftment analysis in PB, BM, and dorsal skin by FACS. The distribution of residual AML cells in dorsal skin was visualized by confocal imaging.

Skin MPC isolation by FACS

Mouse dorsal skin was minced and digested with 0.2% collagenase II (CLSII Worthington Biochemicals) in PBS supplemented with 20% FBS for 60 min at 37°C. After washing with PBS/20% FBS followed by PBS, the digested skin tissue was treated with 0.05% trypsin-EDTA (GIBCO) for 10–15 min at 37°C. The cell suspension was spun down at 300 *g* for 10 min. Mononuclear cells were then incubated with FcR (CD16/32) antibody and stained with CD45, TER119, CD31, CD44, CD140a, and SCA1 for 15 min at 2–8°C. Dead cells were excluded by propidium iodide (PI) staining. For sorting native skin MPCs, hematopoietic and endothelial populations were firstly excluded (CD45⁻TER119⁻CD31⁻) and Ebf2 gate was then defined based on fluorescence minus one (FMO) using skin mononuclear cells from a non-transgenic mouse. Skin Ebf2⁺ and Ebf2⁻ cells were sorted on a FACS Aria III Sorp (BD Biosciences). See Table S1 for detailed antibody information.

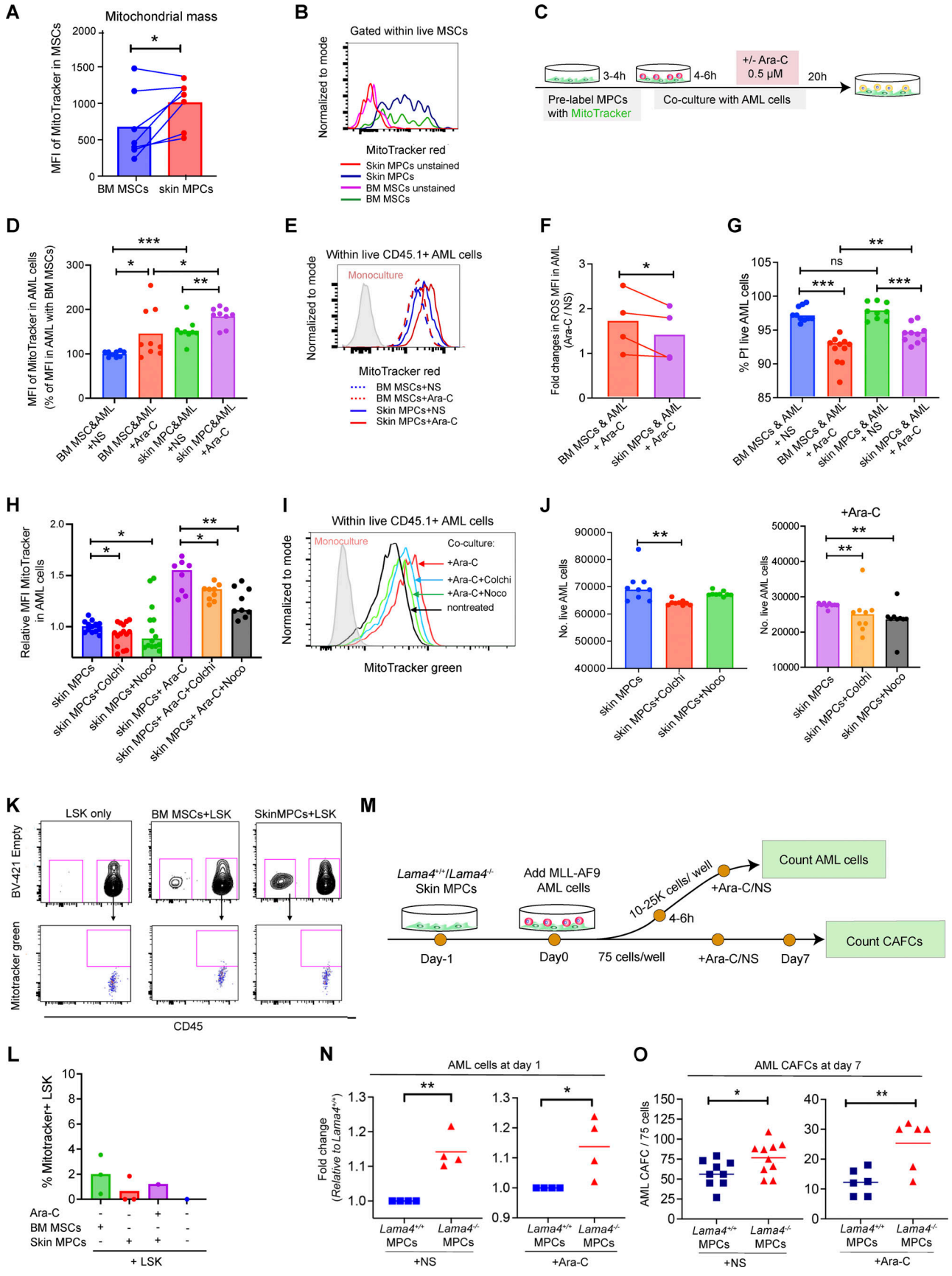

Figure 6. **Mitochondrial transfer and Lama4 deficiency in skin MPCs contributed to the chemoprotection of AML cells from Ara-C. (A and B)** Increased mitochondrial mass in skin MPCs compared to that in BM MSCs. **(A)** MFI of MitoTracker red in BM MSCs and skin PαS MPCs. Each dot represents an individual

assay in triplicate from three independent experiments. *P < 0.05, determined by paired *t* test. **(B)** Representative FACS histograms showing MitoTracker red staining in the skin MPCs and BM MSCs. **(C)** Experimental strategy for determining mitochondrial transfer from stromal cells to AML cells in vitro. Skin MPCs and BM MSCs that were prelabeled with MitoTracker red were cocultured with *MLL-AF9*$^+$ AML cells for 24 h. Ara-C was added 4–6 h after seeding the AML cells. The stromal cell–derived mitochondria were detected by MFI of MitoTracker in the AML cells at 24 h after coculture by FACS. **(D)** MFI of MitoTracker showing increased mitochondrial transfer from skin MPCs to AML cells than that from BM MSCs in the cocultures. Data shown are normalized MitoTracker MFI in the AML cells based on the values of that in the AML cells cocultured with BM MSCs without Ara-C treatment. Each dot represents mean values of three to four replicated measurements in each experiment of four. Horizontal bars are median values. *P < 0.05, **P < 0.01, ***P < 0.001, determined by Kolmogorov–Smirnov test. **(E)** Representative FACS histograms showing MitoTracker staining in the AML cells 24 h after coculture with the stromal cells. The MFI from AML cells in the monoculture without the prelabeled MPCs was used as a negative control. **(F)** Reduced ROS levels in the AML cells cocultured with skin PαS MPCs compared to that with BM MSCs 24 h after Ara-C treatment. Each dot represents the average value of triplicate assays from each experiment of three. Horizontal bars are mean values. *P < 0.05, determined by paired *t* test. **(G)** The percentage of PI$^-$ live AML cells in the cocultures 24 h after Ara-C treatment. Each dot represents mean values of three to four replicated measurements in each experiment of four. Horizontal bars are median values. The statistical differences were determined by unpaired *t* test, ns, no significant difference, **P < 0.01, ***P < 0.001. **(H–J)** Impaired protective mitochondrial transfer from skin MPCs to AML cells in the cocultures after treatment with microtubule inhibitors. **(H)** MFIs of MitoTracker green in AML cells cocultured with skin MPCs and treated with colchicine, nocodazole alone, or in combination with Ara-C. The MFIs were normalized to the nontreated controls, from four independent experiments. Each dot represents a single measurement. *P < 0.05, **P < 0.01, determined by unpaired *t* test. **(I)** Representative histogram showing fluorescence intensity of MitoTracker green in the AML cells. **(J)** The numbers of live AML cells cocultured with skin MPCs after the treatments. **P < 0.01, determined by unpaired *t* test. **(K and L)** Little mitochondrial transfer from skin or BM MSCs to normal BM HSPCs 24 h after coculture. The purified LSK cells were cocultured with MitoTracker green prelabeled skin MPCs for 24 h. The MitoTracker green$^+$ LSK cells were analyzed after coculture based on CD45 expression, as shown in the FACS profile (K and L) the percentage of MitoTracker green$^+$ LSK cells in cocultures and monoculture. Each dot represents a replicate measurement. **(M)** Experimental layout for assessing the impact of *Lama4* loss in skin MPCs for AML growth in vitro using a coculture system. The *Lama4*$^{+/+}$ and *Lama4*$^{-/-}$ skin MPCs were cocultured with *MLL-AF9* AML cells in a 96-well plate. For CAFC assay, Ara-C was added 2 d after seeding of AML cells. The numbers of total AML cells and CAFCs were counted at 24–28 h and day 7 after seeding AML cells, respectively. **(N)** Fold changes in the number of the AML cells in the cocultures with *Lama4*$^{-/-}$ skin MPCs in relation to that with *Lama4*$^{+/+}$ MPCs 24 h after Ara-C or NS treatment. Data were from four independent experiments and each dot represents the mean of triplicate assays. The horizontal bars represent mean values. *P < 0.05, **P < 0.01, determined by paired *t* test. **(O)** The number of CAFCs derived from AML cells in the cocultures with *Lama4*$^{+/+}$ and *Lama4*$^{-/-}$ skin MPCs treated with NS or Ara-C. Data shown are triplicate values from two to three independent experiments. The horizontal bars represent mean values. *P < 0.05, **P < 0.01, determined by unpaired *t* test.

Serial transplantation

To test the leukemia-initiating capacity of the AML cells infiltrated in skin tissue, the AML CD45.1$^+$ cells were sorted from skin tissue of the mice that have developed AML after AML cell injection. The mice were treated with normal saline or Ara-C for 5 d at day 20–21 after AML cell injection. The AML cells in skin were collected 2–3 d after the last injection, sorted by FACS, and transplanted into non-irradiated secondary C57BL/6J recipient mice via tail vein at a dose of 10, 100, 1,000, or 5,000 cells per mouse. The AML development was monitored by blood analysis using FACS and Sysmex as well as by assessing the general health conditions. The survival rate of the mice was estimated based on the date when the mice were found dead or in moribund status. Bones and blood were collected for determining AML engraftment.

In vivo lineage tracing

This was performed as previously described (Xiao et al., 2018b). Dorsal skin from triple transgenic *Ebf2-Egfp* × *Ebf2-Cre*^{ERT2} × *Rosa26*^{loxp}*Stop*^{loxp}*-Tomato* mice (Xiao et al., 2018b) were collected at 3, 6, and 12 mo after TAM injection. Approximately, 1 × 1 cm of dorsal skin tissue was fixed and embedded in OCT for wholemount immunofluorescence. For evaluating the frequency of Ebf2$^+$ cells and their progeny (Tomato$^+$), 2 × 2 cm of dorsal skin tissue was processed for skin MPC isolation by FACS (BD FACS Aria III). For defining the gates for GFP$^+$ and Tomato$^+$ cells, cells from bitransgenic or single transgenic mice were used as FMO controls. After excluding dead cells by PI staining, the CD45$^-$TER119$^-$CD31$^-$ stromal cells were gated. Subsequently, the CD44$^-$ fractions were divided based on CD140a and SCA1 expression.

Skin MPC expansion and proliferation kinetics in vitro

For in vitro expansion, CFU-Fs from FACS-sorted skin Ebf2$^+$ and Ebf2$^-$PαS cells were trypsinized with 0.05% trypsin-EDTA (GIBCO), collected, and plated to T-25 flasks at 400 cells/cm^2. Cells were then expanded in complete Dulbecco-modified Eagle Medium (DMEM, 31966; GIBCO) containing 10% FBS, 10 mM Hepes (1 M), 100 U of penicillin/streptomycin, and 10^{-4} M 2-mercaptoethanol (M7522; Sigma-Aldrich) under hypoxic condition (1–2% O_2) until 80–90% confluence was reached. Proliferation rates of skin Ebf2$^+$ and Ebf2$^-$PαS cells were evaluated by population doubling time (PDT) assays. PDT was calculated by dividing the number of days for culturing the cells with the number of population doublings (PDs) using the following formula: PDT = Culture time (days)/PD where PD = log (NH/NI)/$\log_2$, NH is the harvested cell number, and NI is the initial cell number.

Dorsal skin wholemount immunofluorescence staining

Dorsal skin specimens were fixed in 4% PFA for 10 min followed by washing with PBS prior to embedding in OCT-Compound (4583; Sakura Tissue Tex). For immunofluorescence staining, 150 µm dorsal skin sections were first blocked with skim milk, fish skin gelatin (G7765; Sigma-Aldrich), and Triton X-100 (T8787; Sigma-Aldrich) for 1 h at room temperature. To visualize Ebf2$^+$ cells in mouse dorsal skin, the sections were incubated with anti-GFP and additionally stained with either anti-mouse MECA32, CD31, NG2, NESTIN, or α-SMA antibodies. All stainings were performed at 2–8°C overnight prior to washing with PBS and stained with secondary antibody. Imaging was performed with confocal microscopy at Live Cell Imaging facility after the section was mounted in Mountant PermaFlour

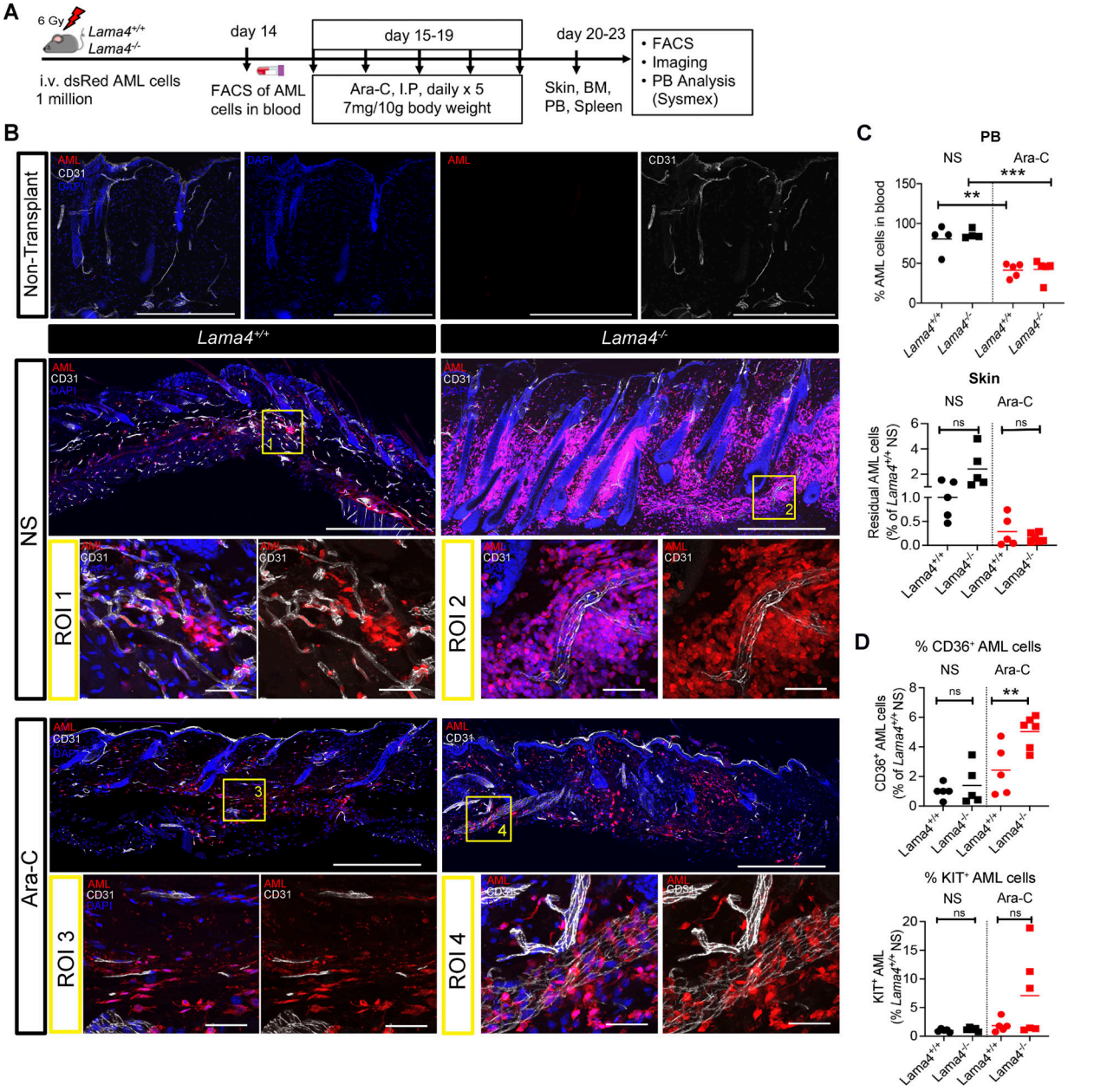

Figure 7. **A high level of residual AML cell infiltration in skin tissue of AML-promoting *Lama4*$^{-/-}$ mouse model post Ara-C treatment. (A)** Experimental setup. *Lama4*$^{+/+}$ and *Lama4*$^{-/-}$ mice were first injected with DsRed-expressing *MLL-AF9* AML cells after sublethal irradiation and treated with NS or Ara-C at day

15 after injection. PB and BM were collected for FACS and confocal microscopy at 1 d after NS or Ara-C treatment. **(B)** Representative confocal images showing residual AML cells in dorsal skin at 1 d after Ara-C treatment. Scale bars are 500 µm in the panoramic images and 50 µm in the ROI images. **(C)** Frequency of AML cells in PB and skin at 1 d after Ara-C treatment. **(D)** Proportion of $CD36^+$ and KIT^+ AML LSCs in skin at 1 d after Ara-C treatment. Data were from two to five experiments and each dot in C and D represents data from a single mouse. The horizontal bars represent the mean values. n = 5–6 per group. **P < 0.01, ***P < 0.001, determined by unpaired t test. **(E)** Experimental layout for assessing homing of the AML cells into *Lama4*$^{+/+}$ and *Lama4*$^{-/-}$ mice 3 h after transplantation. $CD45.1^+$ *MLL-AF9*$^+$ AML cells (10 million per mouse) were transplanted into the mice via tail vein injection without prior irradiation. Dorsal skin, bones, blood of the recipient mice were harvested 3 h after AML cell transplantation and the homing of the $CD45.1^+$ AML cells was examined by FACS based on CD45.1 expression. **(F)** Representative FACS profiles showing the gatings of $CD45.1^+$ AML cells and $CD45.2^+$ host cells. The gate for $CD45.1^+$ cells was determined based on the FMO control without CD45.1 staining. **(G)** The frequencies of the AML cells in total live cells in the recipient skin and blood. ns, no significant difference, determined by unpaired t test. The horizontal bars represent mean values. Each dot represents individual recipient mouse, n = 3–4 per group. **(H)** The frequencies of the AML cells of total live cells in the *Lama4*$^{+/+}$ and *Lama4*$^{-/-}$ recipient skin and BM. ns, no significant difference, determined by unpaired t test. The horizontal bars represent mean values. Each dot represents an individual recipient mouse.

(TA-030-F19; Thermo Fisher Scientific). See Table S2 for antibodies used for the confocal imaging.

Quantification of the $Ebf2^+$ or Ebf2/$GFP^-Tomato^+$ cells expressing NESTIN, NG2, or α-SMA was performed with NIS-element AR-analysis ver 5.20.00 64-bit software (Nikon). From 100-µm sections, 30–40 µm thickness was scanned with a confocal microscope to localize $Ebf2^+$ and $Ebf2^+$ progenies (Ebf2/$GFP^-Tomato^+$ cells). Areas where $Ebf2^+$ and Ebf2/$GFP^-Tomato^+$ cells were distributed were further imaged every 1–1.1 µm depth to obtain region of interest (ROI). Within ROI, positive expression of NESTIN, NG2, or α-SMA was defined based on control sections stained with secondary antibodies only while GFP^+ signal was set based on samples from non-GFP reporter mice. Three to four mice were included for the quantification.

RNA sequencing

Total RNA from freshly sorted skin $Ebf2^+$ cells, skin $Ebf2^-$ PαS cells, and BM MSCs were isolated with RNeasy Micro Kit (Qiagen) according to the manufacturer's protocol. cDNA was prepared using SMART-Seq v4 Ultra Low Input RNA Kit for Sequencing (634898; Takara Bio.). The cDNA quality was examined on Agilent TapeStation system (RRID:SCR_019547) using a High Sensitivity D5000 ScreenTape (5067-5592; Agilent). 1 ng cDNA was used for library preparation using *Nextera XT* DNA Library Preparation Kit (FC-131-1024 & FC-131-1096; Illumina). The yield and quality of the amplified libraries were analyzed using Qubit by Thermo Fisher Scientific and the Agilent Tapestation System. The indexed cDNA libraries were sequenced on the Illumina 2000 or Nextseq 550 (Illumina) for a 75-cycle v2 sequencing run generating 75 bp single-end reads. About 7–20 million reads/sample were obtained. Sample quality was assessed using FastQC (v0.11.8) and MultiQC (v1.7). Reads were aligned to a reference built from Ensembl GRCm38 genome sequences using STAR (RRID:SCR_004463, v2.6.1d). All mapped counts to each gene were further calculated by FeatureCounts function from Subread package (Liao et al., 2013) installed in R. Genes with reads per kilobase of transcript per million mapped reads values more than 0.1 were considered as being actively transcribed and proceeded to the analysis of differential gene expression (Mortazavi et al., 2008). The normalized read counts assigned to each sample were generated by Deseq2 (RRID: SCR_015687). The differentially expressed genes between the cell subsets were identified by adjusted P value (Padj < 0.05) using Benjamini-Hochberg correction for multiple testing, together with thresholds at $\log_2$fold changes >1 (upregulated) or <−1 (downregulated). For the Gene Set Enrichment Analysis (GSEA), the normalized read counts were imported into the GSEA (v4.0.3) platform from Broad Institute (http://www.broadinstitute.org/gsea/index.jsp), with three gene sets being tested, including gene ontology (c5.all.v5.symbols.gmt), hallmark (h.all.v5.symbols.gmt), and Kyoto Encyclopedia of Genes and Genomes (c2.kegg.v5.symbols.gmt). Gene sets tested were considered to be statistically enriched when the nominal P value <0.01 and false discovery rate < 0.25.

CAFC assay using primary skin MPCs

This was done as previously described (Cai et al., 2022; van Os et al., 2008). Briefly, 30,000 skin/BM MPCs were first plated into a 24-multiwell plate and maintained in complete DMEM (31966; GIBCO) containing 10% FBS, 10 mM Hepes (1 M), 100 U of penicillin/streptomycin, and 10^{-4}M 2-mercaptoethanol (M7522; Sigma-Aldrich) under hypoxic condition (1% O_2). 1 d after, 150–300 MLL-AF9 AML or LSK cells were then added on the stromal cells in Myelocult (M5300; Stem Cell Technologies) with 10^{-6} M hydrocortisone (07904; Stem Cell Technologies), 1% penicillin/streptomycin, and 1 ng/ml IL-3 (R&D). The cocultures were performed at 32°C in 5% CO_2 for 7–14 d. A CAFC was defined as a cluster of more than three cells underneath the MSCs/MPCs. The CAFCs were visualized and scored with an inverted microscope (CKX41; Olympus) on days 7 and 10. The cells were thereafter trypsinized and collected for FACS.

Detection of ROS level and mitochondrial transfer

This was done as recently described (Cai et al., 2022). The MSCs/MPCs or AML cells were harvested and washed with PBS and incubated with 2 µM of H_2-DCFDA (C6827; Thermo Fisher Scientific) in DMEM at 37°C for 40 min to detect ROS level. The cells were then rinsed twice with PBS and resuspended with 150 µl of PI (1:1,000) in 5% FBS/PBS. ROS levels were measured by FACS.

For mitochondrial transfer, MSCs or MPCs were stained with 100 nM MitoTracker red or green FM (M22426 or M7514; Thermo Fisher Scientific) at 37°C for 40 min, according to the manufacturer's instructions. The cells were washed twice with PBS, then incubated for 3–4 h to remove unbound probe before a final wash. Subsequently, 15,000–25,000 *MLL-AF9* AML cells in Myelocult (M5300; StemCell Technologies) were plated and cocultured with prelabeled MSCs for 24 h. Mitochondrial transfer was quantified in AML cells ($CD45.1^+$) by FACS and analyzed for mean fluorescence intensity of the MitoTracker red.

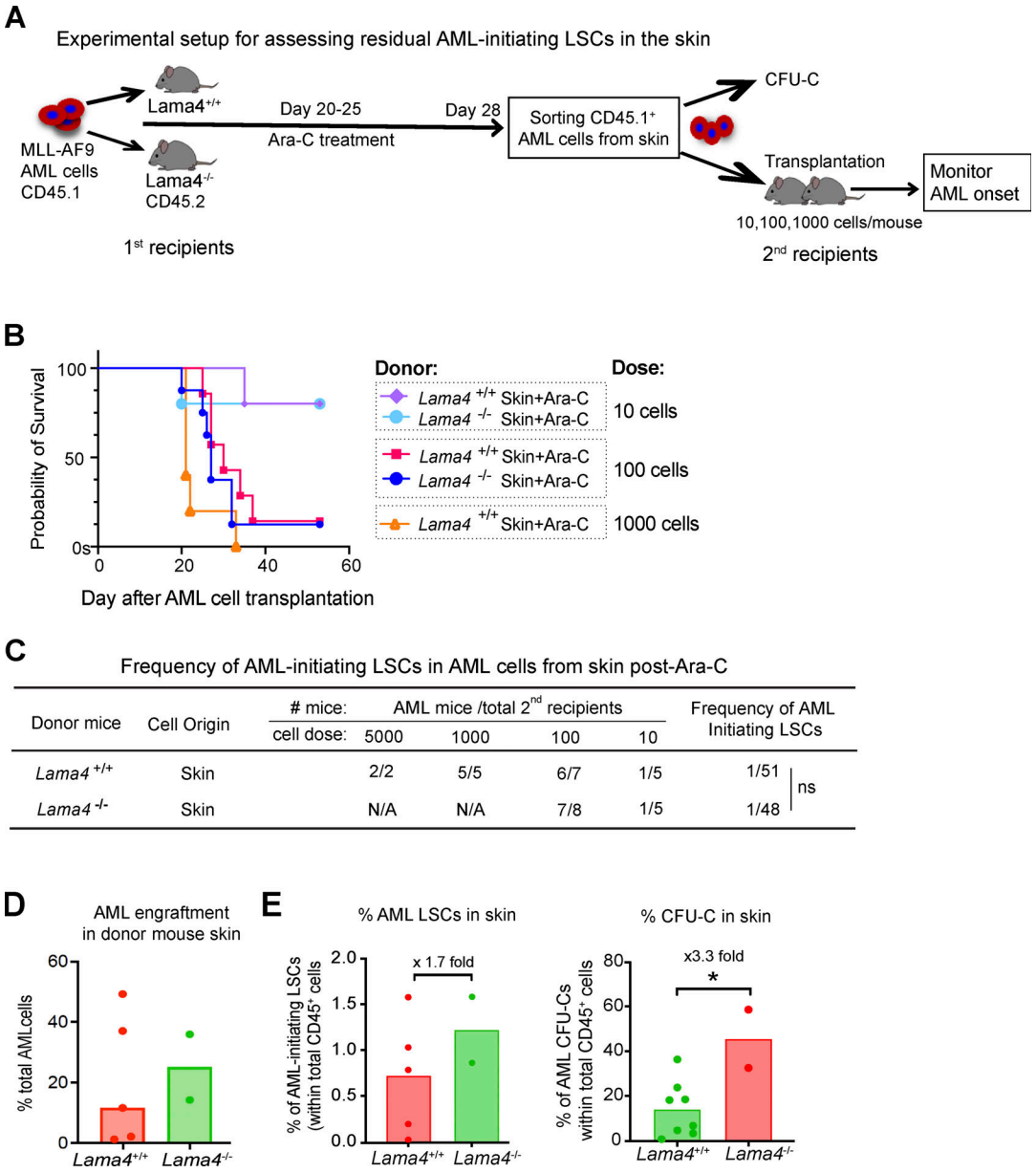

Figure 8. **Serial transplantation indicated more residual AML-initiating LSCs in the *Lama4*$^{-/-}$ mouse skin after Ara-C treatment. (A)** Experimental setup for determining the residual AML-initiating LSCs in the skin of *Lama4*$^{+/+}$ and *Lama4*$^{-/-}$ mice. The mice were injected with *MLL-AF9* AML cells and treated with NS or Ara-C at day 20 after AML cell injection. The CD45.1^{+} AML cells were sorted from the skin at 3 d after Ara-C treatment and intravenously transplanted in limiting cell doses (10, 100, 1,000 cells/mouse) into secondary recipients without prior irradiation. The AML onset was monitored by FACS of AML cells in blood, spleen, and BM. **(B)** The Kaplan-Meier survival curve of the secondary recipient mice that received skin-derived AML cells sorted from primary recipients after treatment with Ara-C. The dates were the days when the mice were found dead or moribund. The survival curve was generated by Log-rank (Mantel–Cox test). *n* = 5–8 per group. **(C)** The frequencies of AML-initiating LSCs in the *Lama4*$^{+/+}$ and *Lama4*$^{-/-}$ mouse skin after Ara-C treatment. The frequency was determined by extreme limiting dilution analysis based on the frequencies of the secondary mice that developed AML (Hu and Smyth, 2009). ns, no significant difference, determined by *Chi square* test. **(D)** The percentage of total AML cells in the skin of the donor *Lama4*$^{+/+}$ and *Lama4*$^{-/-}$ mice. Each dot represents data from a single mouse. The horizontal bars represent the median values. **(E)** The percentage of AML-initiating LSCs (left) and CFU-Cs (right) within total CD45^{+} cells in the skin. The data were calculated based on percentage of AML cells in skin and the frequency (C) of the LSCs and CFU-Cs, respectively. Each dot represents data from a single primary recipient mouse. The horizontal bars represent the mean values. *P < 0.05, determined by unpaired *t* test. Data were from two transplantation experiments.

Multilineage differentiation assay

This was done as described (Xiao et al., 2018b). The skin Ebf2^{+}, Ebf2^{-}, and Ebf2^{-}PαS cells were expanded in culture and plated at 400 cells/cm^{2} to each well of a 24-well plate. For osteogenic differentiation, cells were cultured with complete osteogenic medium mixed with human/mouse StemXVivo osteogenic/adipogenic base medium (CCM007; R&D Systems) and mouse StemXVivo osteogenic supplement (CCM009; R&D Systems) under normoxic condition for 14–21 d. Differentiation toward osteoblast was evaluated by 1% alizarin red S (A5533; Sigma-

Aldrich) staining after cell fixation with cold methanol. For adipogenic differentiation, the culture was performed with DMEM containing 10% FBS, 10 mM Hepes (1 M), 100 U of penicillin/streptomycin, 10^{-4} M 2-mercaptoethanol (M7522; Sigma-Aldrich), 5 µg/ml insulin (I6634; Sigma-Aldrich), 20 µM Indomethacin (I7378; Sigma-Aldrich), 0.0115 mg/ml isobutylmethylxanthine (I-7018; Sigma-Aldrich), and 10^{-6} M dexamethasone (D2915; Sigma-Aldrich) for 2–3 wk. Cells were first stained with 500 µl of 2 µM of Bodipy 500/510 (D3823; Invitrogen) for imaging live adipocytes, then fixed with 10% formalin, and stained with 0.5% Oil Red O (O1391; Sigma-Aldrich). Chondrogenic differentiation was induced in monolayer culture where cells were cultured at 37°C under hypoxic conditions (2% O_2) with DMEM high glucose containing 10 mM Hepes (1 M), 100 U of penicillin/streptomycin, 10^{-4} M 2-mercaptoethanol (M7522; Sigma-Aldrich), 2 mM pyruvate (P5280; Sigma-Aldrich), 0.35 mM *L*-proline (P5607-25G; Sigma-Aldrich), ITS^{+3} (I-3146; Sigma-Aldrich), 5 µg/ml *L*-ascorbic acid 2-phosphate (A7506; Sigma-Aldrich), 10^{-7} M dexamethasone (D2915; Sigma-Aldrich), and 10 ng/ml TGF-β3 (100-36E; Peprotech). To assess chondrogenic differentiation, toluidine blue (T3260; Sigma-Aldrich; pH 2.0–2.5) was used to stain proteoglycan. Images were then taken under an inverted microscope (CKX41; Olympus).

In vitro chondrogenic induction in micromass pellet

After in vitro expansion, 2.5 × 10^5 of BM MSCs or skin $Ebf2^+$ or skin $Ebf2^-$PαS MPCs were collected in a 15-ml tube and spun down at 300 *g* for 7 min. After removal of supernatant, 500 µM of chondrogenic medium consisting of DMEM high glucose with 10 mM Hepes, 100 U of penicillin/streptomycin, 10^{-4} M 2-Mercaptoethanol (M7522; Sigma-Aldrich), 2 mM pyruvate (P5280; Sigma-Aldrich), 0.35 mM *L*-proline (P5607-25G; Sigma-Aldrich), ITS^{+3} (I-3146; Sigma-Aldrich), 5 µg/ml *L*-ascorbic acid 2-phosphate (A7506; Sigma-Aldrich), 10^{-7} M dexamethasone (D2915; Sigma-Aldrich), and 10 ng/ml TGF-β3 (100-36E; Peprotech) were added. The chondrogenic induction was performed at 37°C under hypoxic conditions (2% O_2). Every 2–3 d, the medium was replaced until day 28. For evaluating the chondrogenic induction, the micromass pellets were washed with PBS prior to being fixed in 4% PFA for 2 d. After dehydration with 70% ethanol, the pellets were stained with toluidine blue (T3260; Sigma-Aldrich) at pH 2.0–2.5 for 15–30 min. Thereafter, the stained pellets were washed with 70% ethanol and embedded in OCT-compound (4583; Sakura Tissue Tex). To visualize the formation of proteoglycan, the embedded pellet was cut to 10 µm, mounted, and observed by an inverted microscope (Axio Observer.Z1; Zeis). Images were processed with Zen software (GmbH 2011; Carl Zeiss Microscopy).

$LSKCD150^+$ cell isolation

The $LSKCD150^+$ HSCs were isolated from femurs and tibias of young adult mice, as described (Xiao et al., 2018a). See Table S1 for antibody detail information.

Coculture of skin MPCs with $LSKCD150^+$ cells and CFU-C assay

25,000 expanded $Ebf2^+$ or $Ebf2^-$PαS MPCs from skin and BM at passages 4–13 were plated into each well of a 12-well plate and maintained in complete DMEM (31966; GIBCO) containing 10% FBS, 10 mM Hepes (1 M), 100 U of penicillin/streptomycin, and 10^{-4} M 2-mercaptoethanol (M7522; Sigma-Aldrich) under hypoxic conditions (2% O_2) for 24 h prior to coculture. The cocultures were started by plating 2,000 sorted $LSKCD150^+$ to each well in Myelocult medium (M5300; Stem Cell Technologies) supplemented with 10^{-6} M hydrocortisone (74142; Stem Cell Technologies) and 1% penicillin/streptomycin. After a 3-d coculture in 5% CO_2 at 37°C, the medium containing hematopoietic cells and trypsinized cells were collected for FACS analysis and CFU-C assay in methylcellulose M3434 (Stem Cell Technologies). After 10 d of culture at 37°C in 5% CO_2, the CFU-Cs were stained with 2,7-diaminofluorene and scored with an inverted microscope (CKX41; Olympus). A cell cluster with a minimum of 50 cells is defined as one colony. Colonies with 2,7-diaminofluorene staining were defined as erythrocytes-containing colonies including CFU-granulocyte-macrophage-erythrocyte (GME) and burst-forming unit erythrocyte, as performed (McGuckin et al., 2003; Xiao et al., 2018a).

Quantitative RT-PCR (qPCR)

BM and skin $Ebf2^+$ and $Ebf2^-$ PaS MPCs were freshly sorted into RLT buffer (Qiagen) + 2-Mercaptoethanol and stored at −80°C. RNA extraction was performed with RNeasy Micro Kit (Qiagen) by following the manufacturer's protocol. To synthesize cDNA, RNA was reverse transcribed using SuperScript IV (Invitrogen) and random primer (Invitrogen). qPCR was performed with Biorad C1000 after mixing cDNA with 2x Taqman universal PCR master mix, RNase-free H_2O, and 20xTaqMan primer-probe mix (Invitrogen). See Table S3 for information of Assays-on-Demand probes.

Statistical analysis

Unless mentioned, either unpaired *t* test or Mann–Whitney test was used to determine the difference between the groups or cell subsets. All statistical tests were performed with GraphPad Prism 8 software (RRID: SCR_002798), with $P < 0.05$ considered statistically significant.

Online supplemental material

Fig. S1 shows AML cell distribution, absolute numbers in skin, BM, spleen, and blood from AML mice under steady state and after chemotherapy. Fig. S2 illustrates in vitro expansion and differentiation of the Skin $Ebf2^+$ and $Ebf2^-$PαS cell subsets. Fig. S3 provides additional evidence for the perivascular location and expression of α-SMA and NG2 of skin $Ebf2^+$ cells. Fig. S4 shows additional data from lineage-tracing studies suggesting that skin $Ebf2^+$ cells generated $Ebf2^-$ cells while maintaining themselves in vivo. Fig. S5 shows the data from in vitro coculture experiments indicating that skin MPCs have a similar hematopoiesis-supportive function to BM MSCs. Table S1 is a list of antibodies used for flow cytometry. Table S2 is a list of antibodies used for fluorescence staining. Table S3 is a list of probes used for qPCR.

Data availability

The RNA sequencing data in Fig. 5 are available at GEO under accession number GSE167562. All other data are available in the article or upon reasonable request to the corresponding author.

Acknowledgments

We thank Tina Jacob, Karl Annusver, and Alexandra Are from the Department of Cell and Molecular Biology, Karolinska Institute, Sweden, for valuable advice and technical discussion. We thank Alexandre Piccini, Yuanyuan Zhang, and Andranik Durguryan in our group for technical help with the cell culture. We also thank Prof. Marja Ekblom, Lund University for her scientific input. We also would like to thank the core facility at NEO, Bioinformatics and Expression Analysis, which is supported by the board of research at the Karolinska Institute and the research committee at the Karolinska Hospital.

This study was supported by the Swedish Research Council (2019-01361, 2022-01228), Swedish Childhood Cancer Society (PR2015-0142, FoAss13/015, PR2017/0154, PR2020-0166), Swedish Cancer Society (CAN2017/774, 19 0092 SIA, and 20 1222PjF), Åke Olsson foundation, Radiumhemmets Forskningsfonder (151241, 171162, 191253), Karolinska Institute Wallenberg Institute for Regenerative Medicine, Karolinska Institute doctoral education funding (2-1293/2014, 2021-00480), Stiftelsen Clas Groschinskys Minnesfond (ref:M16 50), Cancer Research Karolinska Institute, and Incyte Biosciences Nordic to H. Qian, and the Swedish Research Council (2018-02963) and Swedish Cancer Society (CAN 2018/793) to M. Kasper. FACS analysis and cell sorting were performed at MedH Flow Cytometry core facility (Karolinska Institute), supported by Karolinska Institute/SLL. The confocal images were obtained at the Live Cell Imaging facility/Nikon Center of Excellence, Karolinska Institute, supported by grants from the Knut and Alice Wallenberg Foundation, the Swedish Research Council, Karolinska Institute infrastructure, Centre for Innovative Medicine and Jonasson Center at the Royal Institute of Technology. All major computations were performed on resources provided by the Swedish National Infrastructure for Computing through Uppsala Multidisciplinary Center for Advanced Computational Science under Project sens2018540.

Author contributions: L. Sandhow has substantially participated in designing, performing experiments, collecting and analyzing data, and manuscript writing. H. Cai, E. Leonard, P. Xiao, M. Kondo, X. Sun, L. Tomaipitinca, A. Månsson, and A.-S. Johansson performed experiments, collected data, and assisted with data analysis and manuscript editing. M. Kasper provided scientific input and assistance with confocal imaging of skin tissues. M. Järås provided the DsRed-expressing *MLL-AF9* AML cells and scientific input on the manuscript. K. Tryggvason provided *Lama4*$^{-/-}$ mouse models and scientific input. H. Qian designed, performed experiments, collected and analyzed data, and wrote the manuscript. All authors have approved the final version of the manuscript.

Disclosures: The authors declare no competing financial interests.

Submitted: 1 June 2022
Revised: 10 May 2023
Accepted: 29 June 2023

References

Åhsberg, J., P. Xiao, K. Okuyama, R. Somasundaram, T. Strid, H. Qian, and M. Sigvardsson. 2020. Progression of progenitor B-cell leukemia is associated with alterations of the bone marrow micro-environment. *Haematologica*. 105:e102–e106. https://doi.org/10.3324/haematol.2018.214031

Alonso, S., M. Su, J.W. Jones, S. Ganguly, M.A. Kane, R.J. Jones, and G. Ghiaur. 2015. Human bone marrow niche chemoprotection mediated by cytochrome P450 enzymes. *Oncotarget*. 6:14905–14912. https://doi.org/10.18632/oncotarget.3614

Arai, F., A. Hirao, M. Ohmura, H. Sato, S. Matsuoka, K. Takubo, K. Ito, G.Y. Koh, and T. Suda. 2004. Tie2/angiopoietin-1 signaling regulates hematopoietic stem cell quiescence in the bone marrow niche. *Cell*. 118: 149–161. https://doi.org/10.1016/j.cell.2004.07.004

Armulik, A., G. Genové, and C. Betsholtz. 2011. Pericytes: Developmental, physiological, and pathological perspectives, problems, and promises. *Dev. Cell*. 21:193–215. https://doi.org/10.1016/j.devcel.2011.07.001

Bakst, R.L., M.S. Tallman, D. Douer, and J. Yahalom. 2011. How I treat extramedullary acute myeloid leukemia. *Blood*. 118:3785–3793. https://doi.org/10.1182/blood-2011-04-347229

Baryawno, N., D. Przybylski, M.S. Kowalczyk, Y. Kfoury, N. Severe, K. Gustafsson, K.D. Kokkaliaris, F. Mercier, M. Tabaka, M. Hofree, et al. 2019. A cellular taxonomy of the bone marrow stroma in homeostasis and leukemia. *Cell*. 177:1915–1932.e1916. https://doi.org/10.1016/j.cell.2019.04.040

Batsivari, A., M.L.R. Haltalli, D. Passaro, C. Pospori, C. Lo Celso, and D. Bonnet. 2020. Dynamic responses of the haematopoietic stem cell niche to diverse stresses. *Nat. Cell Biol.* 22:7–17. https://doi.org/10.1038/s41556-019-0444-9

Cai, H., M. Kondo, L. Sandhow, P. Xiao, A.S. Johansson, T. Sasaki, J. Zawacka-Pankau, K. Tryggvason, J. Ungerstedt, J. Walfridsson, et al. 2022. Critical role of Lama4 for hematopoiesis regeneration and acute myeloid leukemia progression. *Blood*. 139:3040–3057. https://doi.org/10.1182/blood.2021011510

Calvi, L.M., G.B. Adams, K.W. Weibrecht, J.M. Weber, D.P. Olson, M.C. Knight, R.P. Martin, E. Schipani, P. Divieti, F.R. Bringhurst, et al. 2003. Osteoblastic cells regulate the haematopoietic stem cell niche. *Nature*. 425:841–846. https://doi.org/10.1038/nature02040

Dong, L., W.M. Yu, H. Zheng, M.L. Loh, S.T. Bunting, M. Pauly, G. Huang, M. Zhou, H.E. Broxmeyer, D.T. Scadden, and C.K. Qu. 2016. Leukaemogenic effects of Ptpn11 activating mutations in the stem cell microenvironment. *Nature*. 539:304–308. https://doi.org/10.1038/nature20131

Duarte, D., E.D. Hawkins, O. Akinduro, H. Ang, K. De Filippo, I.Y. Kong, M. Haltalli, N. Ruivo, L. Straszkowski, S.J. Vervoort, et al. 2018. Inhibition of endosteal vascular niche remodeling rescues hematopoietic stem cell loss in AML. *Cell Stem Cell*. 22:64–77.e6. https://doi.org/10.1016/j.stem.2017.11.006

Farge, T., E. Saland, F. de Toni, N. Aroua, M. Hosseini, R. Perry, C. Bosc, M. Sugita, L. Stuani, M. Fraisse, et al. 2017. Chemotherapy-resistant human acute myeloid leukemia cells are not enriched for leukemic stem cells but require oxidative metabolism. *Cancer Discov*. 7:716–735. https://doi.org/10.1158/2159-8290.CD-16-0441

Forte, D., M. García-Fernández, A. Sánchez-Aguilera, V. Stavropoulou, C. Fielding, D. Martín-Pérez, J.A. López, A.S.H. Costa, L. Tronci, E. Nikitopoulou, et al. 2020. Bone marrow mesenchymal stem cells support acute myeloid leukemia bioenergetics and enhance antioxidant defense and escape from chemotherapy. *Cell Metab*. 32:829–843.e9. https://doi.org/10.1016/j.cmet.2020.09.001

Gouache, E., V. Greze, M. Strullu, P. Saultier, O. Fenneteau, V. Gandemer, C. Ragu, A. Auvrignon, H. Boutroux, H. Lapillonne, et al. 2018. Leukemia cutis in childhood acute myeloid leukemia: Epidemiological, clinical, biological, and prognostic characteristics of patients included in the ELAM02 study. *HemaSphere*. 2:e141. https://doi.org/10.1097/HS9.0000000000000141

Greenbaum, A., Y.M. Hsu, R.B. Day, L.G. Schuettpelz, M.J. Christopher, J.N. Borgerding, T. Nagasawa, and D.C. Link. 2013. CXCL12 in early mesenchymal progenitors is required for haematopoietic stem-cell maintenance. *Nature*. 495:227–230. https://doi.org/10.1038/nature11926

Gu, Y.C., J. Kortesmaa, K. Tryggvason, J. Persson, P. Ekblom, S.E. Jacobsen, and M. Ekblom. 2003. Laminin isoform-specific promotion of adhesion and migration of human bone marrow progenitor cells. *Blood*. 101: 877–885. https://doi.org/10.1182/blood-2002-03-0796

Han, J., Y.J. Koh, H.R. Moon, H.G. Ryoo, C.H. Cho, I. Kim, and G.Y. Koh. 2010. Adipose tissue is an extramedullary reservoir for functional hematopoietic stem and progenitor cells. *Blood*. 115:957–964. https://doi.org/10.1182/blood-2009-05-219923

Hanoun, M., D. Zhang, T. Mizoguchi, S. Pinho, H. Pierce, Y. Kunisaki, J. Lacombe, S.A. Armstrong, U. Dührsen, and P.S. Frenette. 2014. Acute myelogenous leukemia-induced sympathetic neuropathy promotes malignancy in an altered hematopoietic stem cell niche. *Cell Stem Cell*. 15:365–375. https://doi.org/10.1016/j.stem.2014.06.020

Hartwell, K.A., P.G. Miller, S. Mukherjee, A.R. Kahn, A.L. Stewart, D.J. Logan, J.M. Negri, M. Duvet, M. Järås, R. Puram, et al. 2013. Niche-based screening identifies small-molecule inhibitors of leukemia stem cells. *Nat. Chem. Biol.* 9:840–848. https://doi.org/10.1038/nchembio.1367

Hoggatt, J., Y. Kfoury, and D.T. Scadden. 2016. Hematopoietic stem cell niche in health and disease. *Annu. Rev. Pathol.* 11:555–581. https://doi.org/10.1146/annurev-pathol-012615-044414

Hu, Y., and G.K. Smyth. 2009. ELDA: Extreme limiting dilution analysis for comparing depleted and enriched populations in stem cell and other assays. *J. Immunol. Methods*. 347:70–78. https://doi.org/10.1016/j.jim.2009.06.008

Iwamoto, S., K. Mihara, J.R. Downing, C.H. Pui, and D. Campana. 2007. Mesenchymal cells regulate the response of acute lymphoblastic leukemia cells to asparaginase. *J. Clin. Invest.* 117:1049–1057. https://doi.org/10.1172/JCI30235

Jeong, S.Y., J.A. Kim, and I.H. Oh. 2018. The adaptive remodeling of stem cell niche in stimulated bone marrow counteracts the leukemic niche. *Stem Cells*. 36:1617–1629. https://doi.org/10.1002/stem.2870

Jin, L., Y. Tabe, S. Konoplev, Y. Xu, C.E. Leysath, H. Lu, S. Kimura, A. Ohsaka, M.B. Rios, L. Calvert, et al. 2008. CXCR4 up-regulation by imatinib induces chronic myelogenous leukemia (CML) cell migration to bone marrow stroma and promotes survival of quiescent CML cells. *Mol. Cancer Ther.* 7:48–58. https://doi.org/10.1158/1535-7163.MCT-07-0042

Kim, J.A., J.S. Shim, G.Y. Lee, H.W. Yim, T.M. Kim, M. Kim, S.H. Leem, J.W. Lee, C.K. Min, and I.H. Oh. 2015. Microenvironmental remodeling as a parameter and prognostic factor of heterogeneous leukemogenesis in acute myeloid leukemia. *Cancer Res.* 75:2222–2231. https://doi.org/10.1158/0008-5472.CAN-14-3379

Kimlin, L., and V. Virador. 2013. Cellular populations isolated from newborn mouse skin including mesenchymal stem cells. *Methods Mol. Biol.* 989:217–233. https://doi.org/10.1007/978-1-62703-330-5_17

Krooks, J.A., and A.G. Weatherall. 2018. Leukemia cutis in acute myeloid leukemia signifies a poor prognosis. *Cutis*. 102:266–272.

Kusumbe, A.P., S.K. Ramasamy, T. Itkin, M.A. Mäe, U.H. Langen, C. Betsholtz, T. Lapidot, and R.H. Adams. 2016. Age-dependent modulation of vascular niches for haematopoietic stem cells. *Nature*. 532:380–384. https://doi.org/10.1038/nature17638

Landberg, N., S. von Palffy, M. Askmyr, H. Lilljebjörn, C. Sandén, M. Rissler, S. Mustjoki, H. Hjorth-Hansen, J. Richter, H. Ågerstam, et al. 2018. CD36 defines primitive chronic myeloid leukemia cells less responsive to imatinib but vulnerable to antibody-based therapeutic targeting. *Haematologica*. 103:447–455. https://doi.org/10.3324/haematol.2017.169946

Liao, Y., G.K. Smyth, and W. Shi. 2013. The subread aligner: Fast, accurate and scalable read mapping by seed-and-vote. *Nucleic Acids Res.* 41:e108. https://doi.org/10.1093/nar/gkt214

Madapura, H.S., N. Nagy, D. Ujvari, T. Kallas, M.C.L. Kröhnke, S. Amu, M. Björkholm, L. Stenke, P.K. Mandal, J.S. McMurray, et al. 2017. Interferon γ is a STAT1-dependent direct inducer of BCL6 expression in imatinib-treated chronic myeloid leukemia cells. *Oncogene*. 36:4619–4628. https://doi.org/10.1038/onc.2017.85

Manshouri, T., Z. Estrov, A. Quintás-Cardama, J. Burger, Y. Zhang, A. Livun, L. Knez, D. Harris, C.J. Creighton, H.M. Kantarjian, and S. Verstovsek. 2011. Bone marrow stroma-secreted cytokines protect JAK2(V617F)-mutated cells from the effects of a JAK2 inhibitor. *Cancer Res.* 71:3831–3840. https://doi.org/10.1158/0008-5472.CAN-10-4002

Marlein, C.R., L. Zaitseva, R.E. Piddock, S.D. Robinson, D.R. Edwards, M.S. Shafat, Z. Zhou, M. Lawes, K.M. Bowles, and S.A. Rushworth. 2017. NADPH oxidase-2 derived superoxide drives mitochondrial transfer from bone marrow stromal cells to leukemic blasts. *Blood*. 130:1649–1660. https://doi.org/10.1182/blood-2017-03-772939

McGuckin, C.P., N. Forraz, and W.M. Liu. 2003. Diaminofluorene stain detects erythroid differentiation in immature haemopoietic cells treated with EPO, IL-3, SCF, TGFbeta1, MIP-1alpha and IFNgamma. *Eur. J. Haematol.* 70:106–114. https://doi.org/10.1034/j.1600-0609.2003.00009.x

Morikawa, S., Y. Mabuchi, Y. Kubota, Y. Nagai, K. Niibe, E. Hiratsu, S. Suzuki, C. Miyauchi-Hara, N. Nagoshi, T. Sunabori, et al. 2009. Prospective identification, isolation, and systemic transplantation of multipotent mesenchymal stem cells in murine bone marrow. *J. Exp. Med.* 206:2483–2496. https://doi.org/10.1084/jem.20091046

Mortazavi, A., B.A. Williams, K. McCue, L. Schaeffer, and B. Wold. 2008. Mapping and quantifying mammalian transcriptomes by RNA-Seq. *Nat. Methods*. 5:621–628. https://doi.org/10.1038/nmeth.1226

Moschoi, R., V. Imbert, M. Nebout, J. Chiche, D. Mary, T. Prebet, E. Saland, R. Castellano, L. Pouyet, Y. Collette, et al. 2016. Protective mitochondrial transfer from bone marrow stromal cells to acute myeloid leukemic cells during chemotherapy. *Blood*. 128:253–264. https://doi.org/10.1182/blood-2015-07-655860

Omatsu, Y., T. Sugiyama, H. Kohara, G. Kondoh, N. Fujii, K. Kohno, and T. Nagasawa. 2010. The essential functions of adipo-osteogenic progenitors as the hematopoietic stem and progenitor cell niche. *Immunity*. 33:387–399. https://doi.org/10.1016/j.immuni.2010.08.017

Parsi, M., M.S. Go, and A. Ahmed. 2020. Leukemia Cutis. StatPearls, Treasure Island, FL.

Peña-Martínez, P., M. Eriksson, R. Ramakrishnan, M. Chapellier, C. Högberg, C. Orsmark-Pietras, J. Richter, A. Andersson, T. Fioretos, and M. Järås. 2018. Interleukin 4 induces apoptosis of acute myeloid leukemia cells in a Stat6-dependent manner. *Leukemia*. 32:588–596. https://doi.org/10.1038/leu.2017.261

Pinho, S., J. Lacombe, M. Hanoun, T. Mizoguchi, I. Bruns, Y. Kunisaki, and P.S. Frenette. 2013. PDGFRα and CD51 mark human nestin+ sphere-forming mesenchymal stem cells capable of hematopoietic progenitor cell expansion. *J. Exp. Med.* 210:1351–1367. https://doi.org/10.1084/jem.20122252

Poulos, M.G., P. Guo, N.M. Kofler, S. Pinho, M.C. Gutkin, A. Tikhonova, I. Aifantis, P.S. Frenette, J. Kitajewski, S. Rafii, and J.M. Butler. 2013. Endothelial Jagged-1 is necessary for homeostatic and regenerative hematopoiesis. *Cell Rep.* 4:1022–1034. https://doi.org/10.1016/j.celrep.2013.07.048

Qian, H., A. Badaloni, F. Chiara, J. Stjernberg, N. Polisetti, K. Nihlberg, G.G. Consalez, and M. Sigvardsson. 2013. Molecular characterization of prospectively isolated multipotent mesenchymal progenitors provides new insight into the cellular identity of mesenchymal stem cells in mouse bone marrow. *Mol. Cell. Biol.* 33:661–677. https://doi.org/10.1128/MCB.01287-12

Qian, H., K. Le Blanc, and M. Sigvardsson. 2012. Primary mesenchymal stem and progenitor cells from bone marrow lack expression of CD44 protein. *J. Biol. Chem.* 287:25795–25807. https://doi.org/10.1074/jbc.M112.339622

Raaijmakers, M.H., S. Mukherjee, S. Guo, S. Zhang, T. Kobayashi, J.A. Schoonmaker, B.L. Ebert, F. Al-Shahrour, R.P. Hasserjian, E.O. Scadden, et al. 2010. Bone progenitor dysfunction induces myelodysplasia and secondary leukaemia. *Nature*. 464:852–857. https://doi.org/10.1038/nature08851

Schepers, K., E.M. Pietras, D. Reynaud, J. Flach, M. Binnewies, T. Garg, A.J. Wagers, E.C. Hsiao, and E. Passegué. 2013. Myeloproliferative neoplasia remodels the endosteal bone marrow niche into a self-reinforcing leukemic niche. *Cell Stem Cell*. 13:285–299. https://doi.org/10.1016/j.stem.2013.06.009

Somervaille, T.C., and M.L. Cleary. 2006. Identification and characterization of leukemia stem cells in murine MLL-AF9 acute myeloid leukemia. *Cancer Cell*. 10:257–268. https://doi.org/10.1016/j.ccr.2006.08.020

Stier, S., Y. Ko, R. Forkert, C. Lutz, T. Neuhaus, E. Grünewald, T. Cheng, D. Dombkowski, L.M. Calvi, S.R. Rittling, and D.T. Scadden. 2005. Osteopontin is a hematopoietic stem cell niche component that negatively regulates stem cell pool size. *J. Exp. Med.* 201:1781–1791. https://doi.org/10.1084/jem.20041992

Susek, K.H., E. Korpos, J. Huppert, C. Wu, I. Savelyeva, F. Rosenbauer, C. Müller-Tidow, S. Koschmieder, and L. Sorokin. 2018. Bone marrow laminins influence hematopoietic stem and progenitor cell cycling and homing to the bone marrow. *Matrix Biol.* 67:47–62. https://doi.org/10.1016/j.matbio.2018.01.007

Thorén, L.A., K. Liuba, D. Bryder, J.M. Nygren, C.T. Jensen, H. Qian, J. Antonchuk, and S.E. Jacobsen. 2008. Kit regulates maintenance of quiescent hematopoietic stem cells. *J. Immunol.* 180:2045–2053. https://doi.org/10.4049/jimmunol.180.4.2045

Thyboll, J., J. Kortesmaa, R. Cao, R. Soininen, L. Wang, A. Iivanainen, L. Sorokin, M. Risling, Y. Cao, and K. Tryggvason. 2002. Deletion of the laminin alpha4 chain leads to impaired microvessel maturation. *Mol. Cell. Biol.* 22:1194–1202. https://doi.org/10.1128/MCB.22.4.1194-1202.2002

Toma, J.G., M. Akhavan, K.J.L. Fernandes, F. Barnabé-Heider, A. Sadikot, D.R. Kaplan, and F.D. Miller. 2001. Isolation of multipotent adult stem cells from the dermis of mammalian skin. *Nat. Cell Biol.* 3:778–784. https://doi.org/10.1038/ncb0901-778

Vaculik, C., C. Schuster, W. Bauer, N. Iram, K. Pfisterer, G. Kramer, A. Reinisch, D. Strunk, and A. Elbe-Bürger. 2012. Human dermis harbors distinct mesenchymal stromal cell subsets. *J. Invest. Dermatol.* 132: 563–574. https://doi.org/10.1038/jid.2011.355

van Os, R.P., B. Dethmers-Ausema, and G. de Haan. 2008. In vitro assays for cobblestone area-forming cells, LTC-IC, and CFU-C. *Methods Mol. Biol.* 430:143–157. https://doi.org/10.1007/978-1-59745-182-6_10

Viswanathan, S., Y. Shi, J. Galipeau, M. Krampera, K. Leblanc, I. Martin, J. Nolta, D.G. Phinney, and L. Sensebe. 2019. Mesenchymal stem versus stromal cells: International society for cell & gene therapy (ISCT®) mesenchymal stromal cell committee position statement on nomenclature. *Cytotherapy*. 21:1019–1024. https://doi.org/10.1016/j.jcyt.2019.08.002

Wang, C.X., I. Pusic, and M.J. Anadkat. 2019. Association of leukemia cutis with survival in acute myeloid leukemia. *JAMA Dermatol.* 155:826–832. https://doi.org/10.1001/jamadermatol.2019.0052

Welner, R.S., G. Amabile, D. Bararia, A. Czibere, H. Yang, H. Zhang, L.L. Pontes, M. Ye, E. Levantini, A. Di Ruscio, et al. 2015. Treatment of chronic myelogenous leukemia by blocking cytokine alterations found in normal stem and progenitor cells. *Cancer Cell*. 27:671–681. https://doi.org/10.1016/j.ccell.2015.04.004

Xiao, P., M. Dolinska, L. Sandhow, M. Kondo, A.S. Johansson, T. Bouderlique, Y. Zhao, X. Li, M. Dimitriou, G.Z. Rassidakis, et al. 2018a. Sipa1 deficiency-induced bone marrow niche alterations lead to the initiation of myeloproliferative neoplasm. *Blood Adv.* 2:534–548. https://doi.org/10.1182/bloodadvances.2017013599

Xiao, P., L. Sandhow, Y. Heshmati, M. Kondo, T. Bouderlique, M. Dolinska, A.S. Johansson, M. Sigvardsson, M. Ekblom, J. Walfridsson, and H. Qian. 2018b. Distinct roles of mesenchymal stem and progenitor cells during the development of acute myeloid leukemia in mice. *Blood Adv.* 2: 1480–1494. https://doi.org/10.1182/bloodadvances.2017013870

Xu, X., X. Zhang, Y. Liu, L. Yang, S. Huang, L. Lu, S. Wang, Q. Guo, and L. Zhao. 2016. BM microenvironmental protection of CML cells from imatinib through Stat5/NF-κB signaling and reversal by Wogonin. *Oncotarget*. 7:24436–24454. https://doi.org/10.18632/oncotarget.8332

Ye, H., B. Adane, N. Khan, T. Sullivan, M. Minhajuddin, M. Gasparetto, B. Stevens, S. Pei, M. Balys, J.M. Ashton, et al. 2016. Leukemic stem cells evade chemotherapy by metabolic adaptation to an adipose tissue niche. *Cell Stem Cell*. 19:23–37. https://doi.org/10.1016/j.stem.2016.06.001

Zhang, B., M. Li, T. McDonald, T.L. Holyoake, R.T. Moon, D. Campana, L. Shultz, and R. Bhatia. 2013. Microenvironmental protection of CML stem and progenitor cells from tyrosine kinase inhibitors through N-cadherin and Wnt-β-catenin signaling. *Blood*. 121:1824–1838. https://doi.org/10.1182/blood-2012-02-412890

Supplemental material

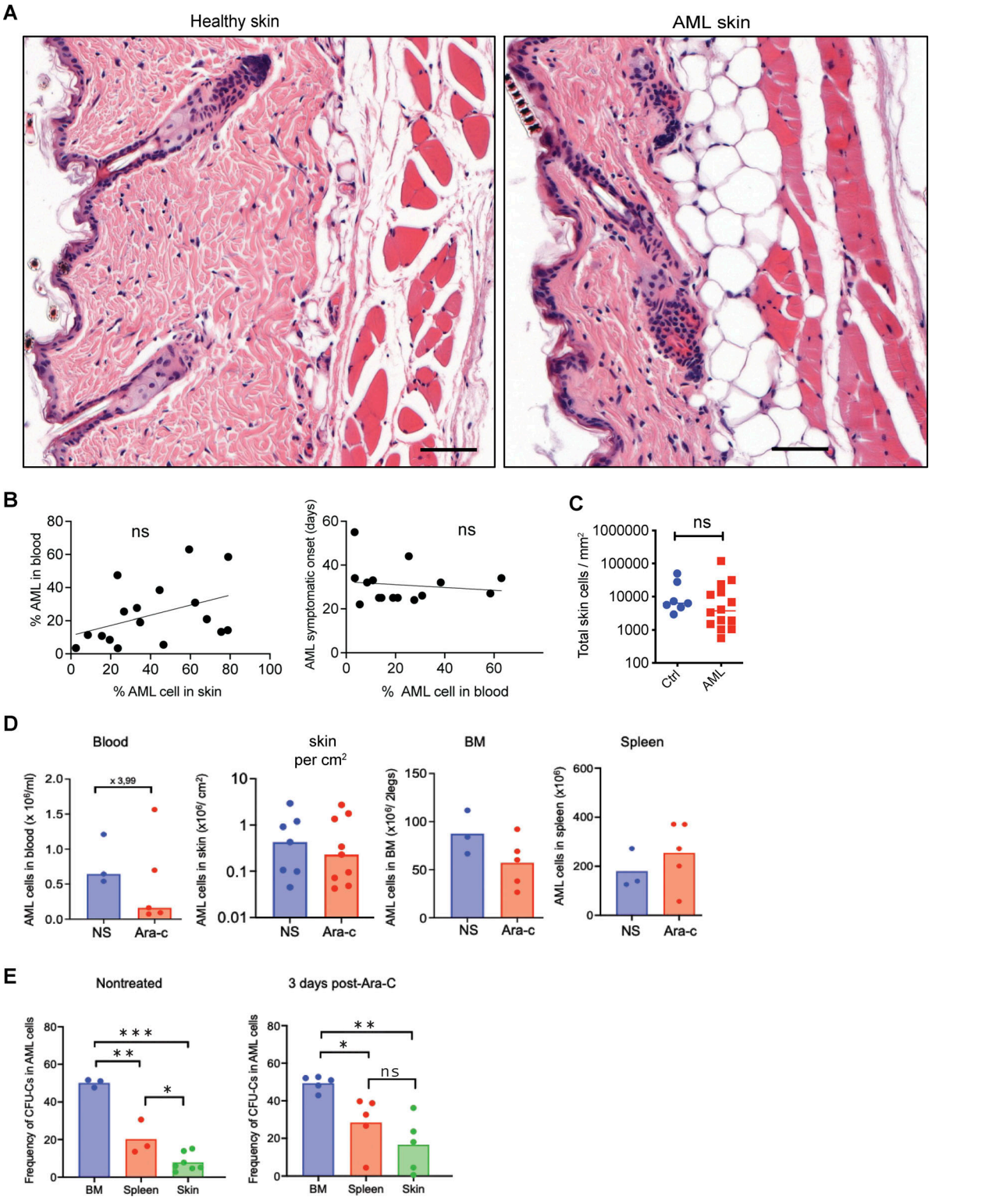

Figure S1. **AML cell distribution in skin, BM, spleen, and blood from AML mice under steady state and after chemotherapy.** Data were from two independent experiments and each dot represents a single mouse with AML. The mice were treated with cytarabine (Ara-C) at day 20 after AML transplantation for 5 d and the AML engraftment was analyzed at 3 d after the treatment. **(A)** Hematoxylin and eosin staining of skin derived from a healthy and AML mouse. Scale bars are 50 µm. **(B)** No significant correlation between AML engraftment in blood and that in the skin (left) or time to AML symptomatic onset (right). No significant difference (ns) was determined by Spearman correlation. **(C)** Total cellularity in the skin of mice with AML and healthy controls (Ctrl). Each dot represents data from one mouse. ns, no significant difference was determined by unpaired *t* test. **(D)** The absolute numbers of AML cells in blood, skin, BM, and spleen. **(E)** The frequency of CFU-Cs derived from the AML cells in BM, skin, and spleen of nontreated (left) and Ara-C–treated (right) mice. The frequencies were calculated based on the frequencies of CFU-Cs within the sorted AML cells and the percent AML cells in each tissue. Each dot represents data from one mouse. *P < 0.05, **P < 0.01, ***P < 0.0001, determined by unpaired *t* test (B, D, left) and paired *t* test (D, right).

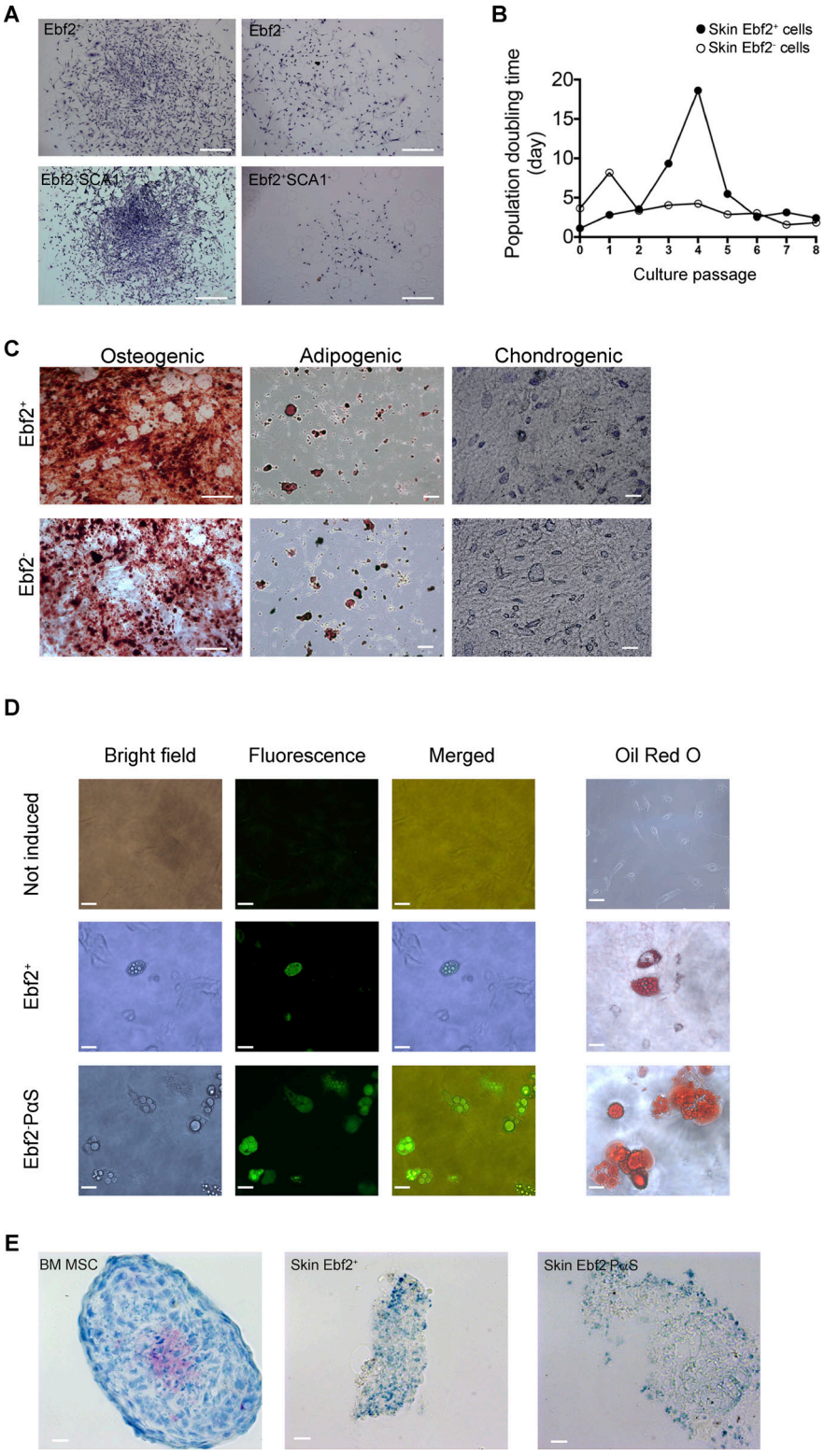

Figure S2. **In vitro expansion and differentiation of the skin Ebf2⁺ and Ebf2⁻ PαS cell subsets. (A)** Images of CFU-Fs derived from the Ebf2⁺ and Ebf2⁻ cell subsets. Scale bars are 500 µm. **(B)** PDT of the skin CD45⁻TER119⁻CD31⁻Ebf2⁺ and Ebf2⁻ stromal cells in culture. PDT was calculated based on culture time (CT)/cell doubling (CD) where CD = log (NH/NI)/log 2, NH is harvested cell number, and NI is the initial cell number. **(C)** Representative images of osteogenic, adipogenic, and chondrogenic differentiation of the skin Ebf2⁺ and Ebf2⁻PαS cells. Scale bars are 500 µm (osteogenic), 100 µm (adipogenic), and 20 µm (chondrogenic). **(D)** Bodipy 500/510 and oil red O staining of differentiated adipocytes from single skin Ebf2⁺ and Ebf2⁻PαS cells–derived CFU-F clones 21 d after the induction. Green and red represent adipocytes stained with bodipy 500/510 and oil red O, respectively. Scale bars are 100 µm. **(E)** Representative images of toluidine blue staining on micromass pellet after chondrogenic induction in vitro. The chondrogenic differentiation in a micromass pellet culture was performed on culture expanded BM MSCs and skin Ebf2⁺ and Ebf2⁻ cell subsets. Scale bars are 20 µm. Related to Fig. 2.

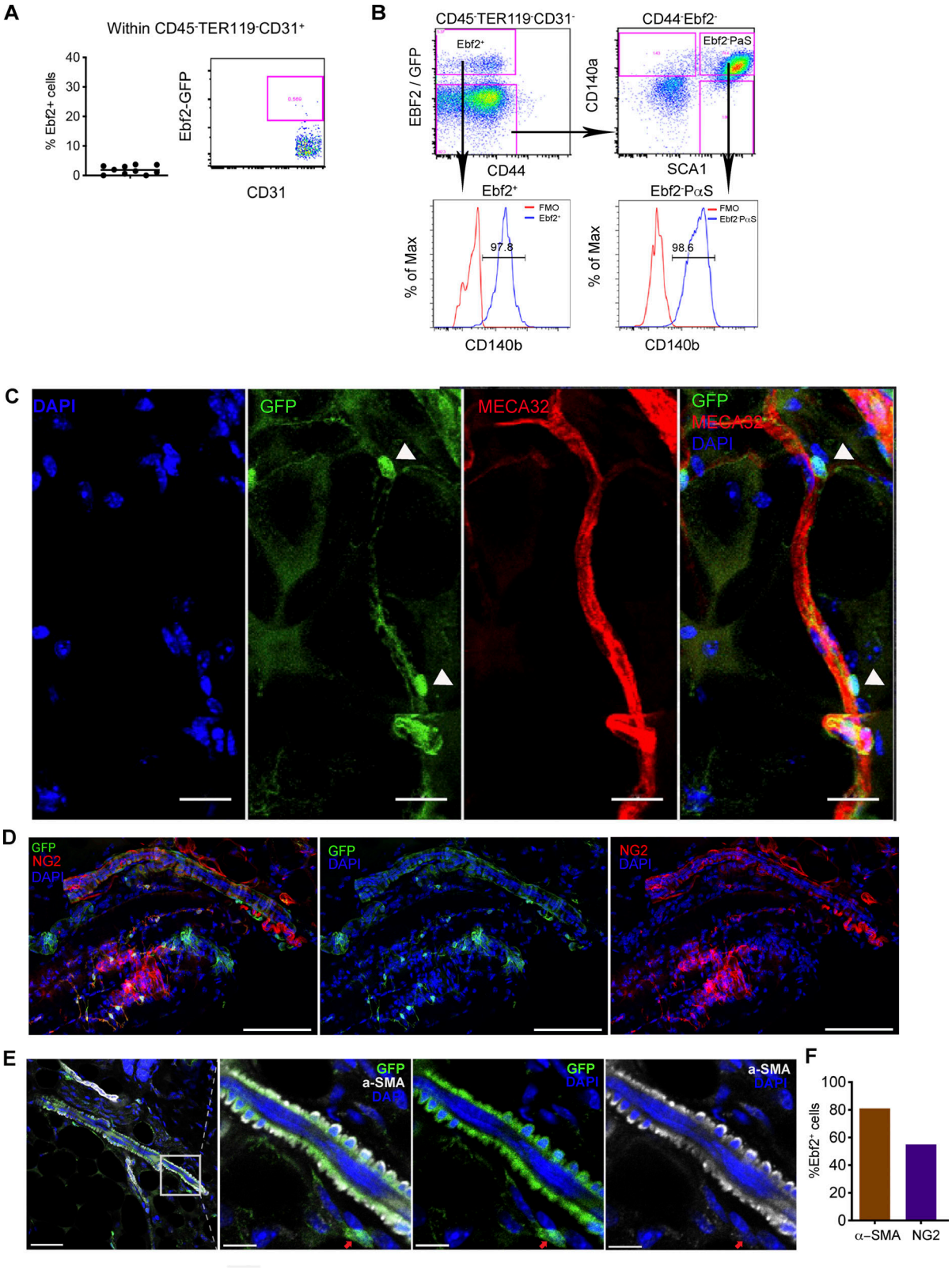

Figure S3. **Skin Ebf2⁺ cells are perivascular cells. (A)** Frequencies of Ebf2⁺ cells expressing CD31. Data are from five sorting experiments. Each dot represents one skin sample from one mouse. **(B)** Representative FACS plots showing analysis of CD140b expression in the skin Ebf2⁺ and Ebf2⁻PαS cells. **(C)** Perivascular localization of Ebf2⁺/GFP⁺ cells. The vessels were identified by MECA32 staining in mouse dorsal skin tissue. The arrowheads indicate Ebf2/GFP⁺ perivascular cells. Scale bars are 20 µm. **(D and E)** Representative images showing localization of Ebf2⁺/GFP⁺ cells in relation to expression of NG2 (D) and α-SMA (E) in skin. Red arrow indicates a Ebf2⁺ cell without α-SMA expression. Scale bars in are 100 µm (D), 50 µm (E, left), and 10 µm (enlarged images in E). **(F)** Quantification of Ebf2⁺/GFP⁺ cells expressing α-SMA and NG2. Data were from three mice. Related to Fig. 3.

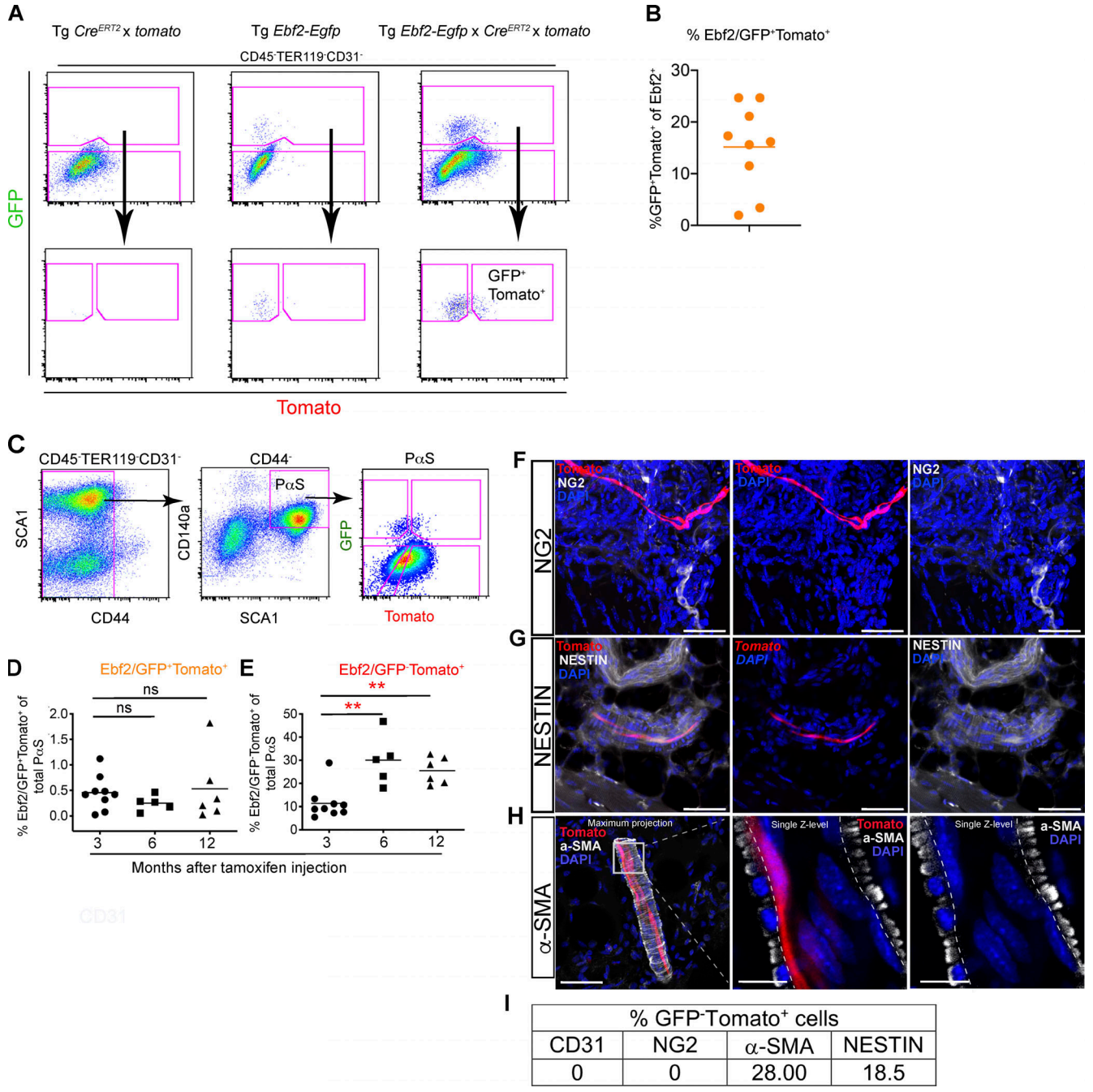

% GFP⁻Tomato⁺ cells			
CD31	NG2	α-SMA	NESTIN
0	0	28.00	18.5

Figure S4. **Skin Ebf2⁺ cells generated Ebf2⁻ cells in vivo. (A)** Representative FACS plot showing the gating of Ebf2/GFP⁺Tomato⁻ and Ebf2/GFP⁺Tomato⁺ cells within skin stromal cells (CD45⁻TER119⁻CD31⁻) at 3 mo after the last TAM injection. Non-transgenic mice were used as controls for background signals of GFP and tomato in samples from Tg *Ebf2-Egfp* × *Cre*^{ERT2}*x tomato* mice. **(B)** The proportion of the Ebf2⁺Tomato⁺ cells within total Ebf2⁺ cells at 3 mo after TAM injection. Each dot represents data from one mouse. Data are from three independent experiments and the horizontal bar represents mean. **(C)** One representative FACS profile showing the Tomato⁺ cell subsets within total CD140a⁺SCA1⁺ (PαS) cells at 3 mo after TAM injection. **(D and E)** Proportion of Ebf2⁺Tomato⁺ (D) and Ebf2⁻Tomato⁺ cells (E) within total PαS MPCs. ns, no significant difference by unpaired *t* test in D. **P < 0.01, by unpaired Mann–Whitney test (E). **(F–H)** Localization of the Tomato⁺ cells in relation to NG2 (F), NESTIN (G), and α-SMA expression (H) at 3 mo after TAM injection. The panorama image was presented as maximum intensity projection and a magnified area was shown as single Z-stack image. Scale bars are 50 µm (F–H left) and 10 µm (enlarged images in H). **(I)** The fractions of Tomato⁺ cells expressing NG2, NESTIN, and α-SMA at 3 mo after TAM injection. Related to Fig. 3.

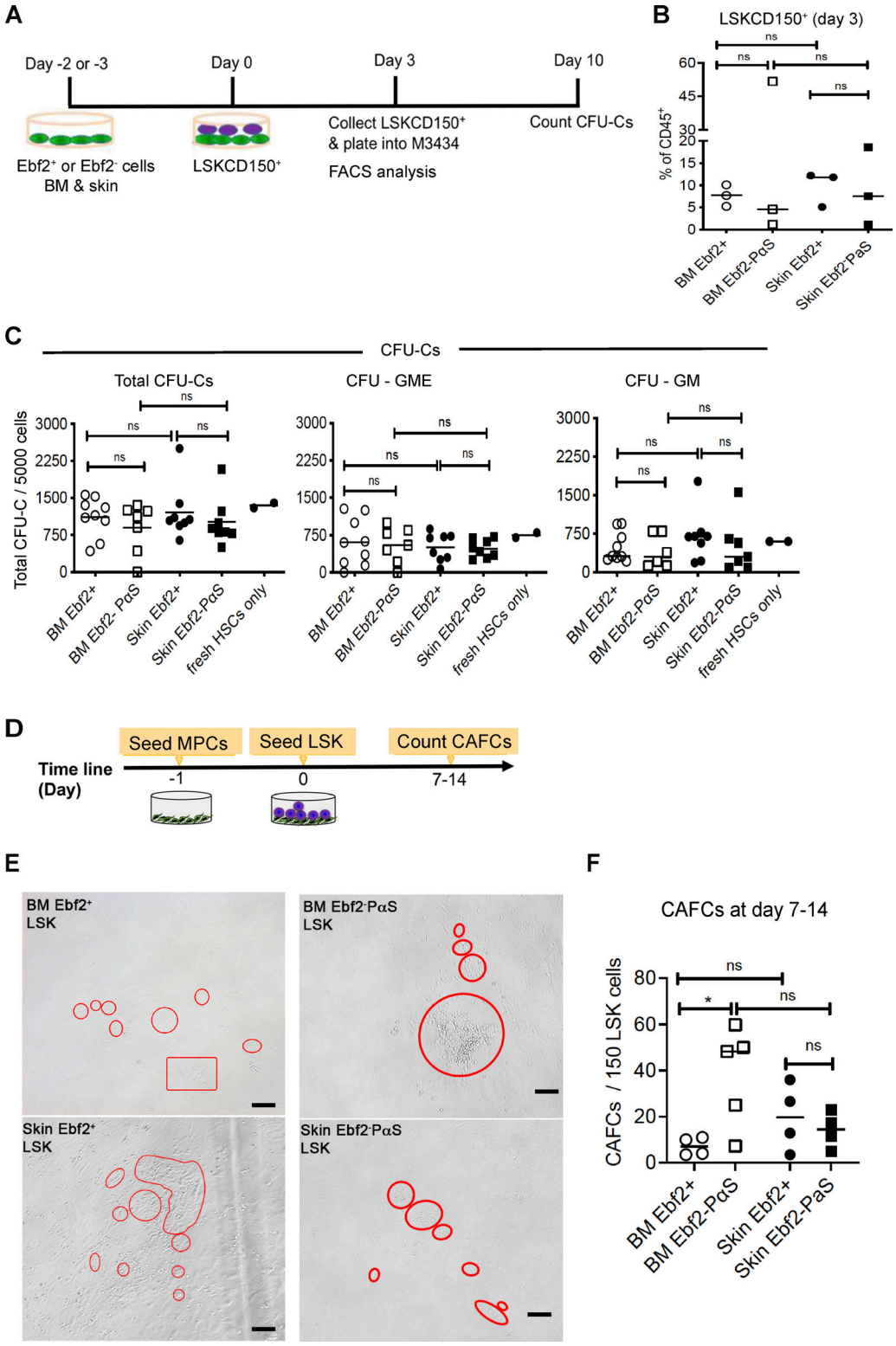

Figure S5. **Skin Ebf2⁺ and Ebf2⁻PαS MPCs exhibit similar hematopoiesis supportive function to BM MSCs. (A)** The experimental layout. LSKCD150⁺ (HSCs) were used for the cocultures with skin MPCs and BM MSC subsets. The cells were analyzed phenotypically at 3 d after the coculture. **(B)** Phenotypical analysis of LSKCD150⁺ HSCs after 3-d coculture with either skin Ebf2⁺ (circle) or Ebf2⁻PαS (square) MPCs or BM MSCs. **(C)** CFU-Cs from LSKCD150⁺ HSCs after being cultured with skin or BM MSCs for 3 d. CFU-granulocyte-macrophage (GM) and CFU-GME were scored at day 10. The CFU-Cs from fresh sorted LSKCD150⁺ HSCs were presented as condition controls. ns, no significant difference by unpaired *t* test. **(D)** The experimental setup for CAFC assay. **(E)** Representative images of the CAFCs from the LSK cells cocultured with the MSCs. Scale bars are 100 µm. **(F)** The numbers of CAFCs after 7–14 d of coculture. Data are presented as mean ± SEM from three to five independent experiments. Each dot represents mean of replicate measurements in each experiment and the horizontal bars represent median values. *P < 0.05, determined by unpaired *t* test was used for statistical analysis. Related to Fig. 4.

Provided online are three tables. Table S1 is a list of antibodies used for flow cytometry. Table S2 is a list of antibodies used for fluorescence staining. Table S3 is a list of probes used for qPCR.